Topologically protected negative entanglement

Wen-Tan Xue1 and Ching Hua Lee1

¹Department of Physics, National University of Singapore, Singapore 117542

The entanglement entropy encodes fundamental characteristics of quantum many-body systems, and is particularly subtle in non-Hermitian settings where eigenstates generically become non-orthogonal. In this work, we find that negative biorthogonal entanglement generically arises from topologically-protected non-orthogonal edge states in free fermion systems, especially within topological flat bands. Departing from previous literature which associated negative entanglement with exceptional gapless points, we show that robustly negative entanglement can still occur in gapped systems. Gapless 2D topological flat bands, however, exhibits novel $S_A \sim -\frac{1}{2}L_y^2\log L$ super volume-law entanglement behavior which scales quadratically with the transverse dimension L_y , independent of system parameters. This dramatically negative scaling can be traced to a new mechanism known as non-Hermitian critical skin compression (nHCSC), where topological and skin localization in one direction produces a hierarchy of extensively many probability non-conserving entanglement eigenstates across a cut in another direction. Our discovery sheds light on new avenues where topology interplays with criticality and non-Hermitian localization, unrelated to traditional notions of topological entanglement entropy. This topologically protected negative entanglement also manifests in the second Rényi entropy, which can be measured through SWAP operator expecation values.

Introduction.— The entanglement entropy plays a crucial role in unveiling fundamental insights into the locality of quantum information. For instance, by scaling either according to the volume or area [1–4], the entanglement entropy reveals whether quantum correlations pervade the entire system or remain localized. Intriguingly, numerous studies [5–7] have suggested that the presence of topological order can also be encoded in the entanglement entropy, as revealed by the presence of an additional constant term [8, 9] or discontinuities [10] in the scaling relation.

In this work, extending into the non-Hermitian realm [11– 53], we uncover a new manner in which topology can substantially influence entanglement entropy behavior. Specifically, we show that certain topological boundary states can exert a strongly non-local influence on the dominant entanglement behavior of the entire system, such probability nonconservation results in negative free-fermion entanglement entropy. A primary feature of non-Hermiticity is that the eigenstates of the Hamiltonian H are generically no longer orthogonal, such that a biorthogonal basis with left and right eigenstates i.e. $H = \sum E_n |\psi_n^R\rangle \langle \psi_n^L|$ with $\langle \psi_m^L | \psi_n^R\rangle = \delta_{mn}$ is needed to maintain orthogonality and retain the probabilistic interpretation of quantum mechanics [54-62]. Within this biorthogonal framework, recent studies have revealed that both bipartite entanglement entropy and Rényi entropy can manifest unexpected negative values [63–70], attributable to the presence of geometric defectiveness at exceptional points (EPs) [66–70].

The first discovery in this work is that the presence of an EP [65] is not strictly a prerequisite for observing negative entanglement entropy values – instead, substantial nonorthogonality among the right eigenstates suffices, and spectacularly so when the non-orthogonality is enforced by a topological flatband. We investigate two 2D topological non-Hermitian models where the topological edge states in these models demonstrate nearly perfect overlap, while the overlap among bulk states remains minimal. Remarkably, this en-

ables topological nontrivialness to be strategically employed to switch the negative entanglement entropy on or off.

Most notably, we discover that non-Hermitian topological flatbands can give rise to unconventional negative supervolume-law entanglement scaling $S_A \sim -\frac{1}{2}L_y^2 \log L$, where L and L_y are respectively the system dimensions normal and parallel to the entanglement cut. This enigmatic $-L_y^2$ scaling dependence arises not just due to the enhanced non-orthogonality of the states due to flatness of the band, but also the extensively many probability-nonconserving entanglement eigenstates that emerge due to the band criticality – in a new mechanism that we dub non-Hermitian critical skin compression (nHCSC).

Negative entanglement from eigenstate non-orthogonality.—In the non-Hermitian context, the density operator that preserves its role as a probabilistic weight is the biorthogonal density matrix $\rho = |\Psi^R\rangle \langle \Psi^L|$, where

$$|\Psi^{R}\rangle = \prod_{n \in occ} \psi_{Rn}^{\dagger} |0\rangle, \quad |\Psi^{L}\rangle = \prod_{n \in occ} \psi_{Ln}^{\dagger} |0\rangle$$
 (1)

are the right and left many-body ground states created by bifermionic creation operators $\psi_{Rn}^{\dagger}, \psi_{Ln}^{\dagger}$ satisfying $\{\psi_{Lm}, \psi_{Rn}^{\dagger}\} = \delta_{mn}$, such that $\langle \Psi^L | \Psi^R \rangle = 1$, even if $\langle \Psi^R | \Psi^R \rangle \neq 1$, $\langle \Psi^L | \Psi^L \rangle \neq 1$. We specialize to free boson and fermion systems, where the ground state and thermal states are Gaussian states. As such, all correlation functions adhere to Wick's theorem, and the reduced density matrix ρ_A corresponding to an entanglement subregion A is completely expressible [71] in terms of the two-point function $\langle c_{x_1}^{\dagger} c_{x_2} \rangle = \langle x_1 | P | x_2 \rangle = L^{-1} \sum_k e^{ik(x_1-x_2)} P(k)$, where [65] $P(k) = \sum_{n \in occ} |\psi_n^R(k)\rangle \langle \psi_n^L(k)|$ projects to the occupied bands n, with k the momentum index. To enforce the entanglement cut, we also introduce Γ_A to be the real-space projector onto subregion A, such that the A-truncated band projector takes the form

$$\bar{P} = \Gamma_A P \Gamma_A = \sum_{n \in occ} \Gamma_A |\psi_n^R\rangle \langle \psi_n^L| \Gamma_A = \sum_{n \in occ} |\psi_{nA}^R\rangle \langle \psi_{nA}^L|. \quad (2)$$

Crucially, this \bar{P} operator crucially contain complete information of the *n*th-order Rényi entropy for free fermions [72]

$$S_A^{(n)} = \frac{\log \text{Tr}(\rho_A^n)}{1 - n} = \frac{1}{1 - n} \text{Tr} \Big[\log \Big(\bar{P}^n + (I - \bar{P})^n \Big) \Big]$$
$$= \frac{1}{1 - n} \sum_i \log(p_i^n + (1 - p_i)^n), \quad (3)$$

which, in the limit of $n \to 1$, yields the von Neumann entropy

$$S_A = -\text{Tr}\rho_A \log \rho_A = -\text{Tr}[\bar{P} \log \bar{P} + (I - \bar{P}) \log(I - \bar{P})]$$

= $\sum_{p_i} -p_i \log(p_i) - (1 - p_i) \log(1 - p_i),$ (4)

where I is the identity matrix and p_i are the eigenvalues of \bar{P} . Physically, p_i represents occupation probabilities subject to the restriction to subregion A, and are indeed real and within [0,1] for Hermitian H. But in non-Hermitian settings, due to the non-conservation of probability across the subregion boundary, we can potentially have $p_i \gg 1$, as we shall show shortly. Importantly, $p_i > 1$ contributes negatively to both $S_A^{(n>1)}$ and $S_A = \lim_{n \to 1} S_A^{(n)}$ entropies, as elaborated in the Supplement [73].

Below, we show that mathematically, it suffices to have strong eigenstate overlap in order to have large p_i , which in turn results in negative Rényi and entanglement entropy. For any pair of non-orthogonal right eigenstates $|\psi_m^R\rangle$ and $|\psi_n^R\rangle$, their normalized squared overlap [74]

$$\eta = \frac{|\langle \psi_m^R | \psi_n^R \rangle|^2}{\langle \psi_m^R | \psi_n^R \rangle \langle \psi_n^R | \psi_n^R \rangle} = \frac{(U^{\dagger} U)_{mn}^2}{(U^{\dagger} U)_{mm} (U^{\dagger} U)_{nn}} \neq 0$$
 (5)

does not vanish. Here we have introduced the matrix U whose elements are the real space components of the right eigenstates i.e. $|\psi_n^R\rangle = \sum_i U_{in}|i\rangle$, such that the corresponding matrix for the left eigenstates is U^{-1} i.e. $\langle\psi_m^L|=\sum_i \left(U^{-1}\right)_{mi}\langle i|$. In the extreme limit where the two eigenstates become parallel, $\eta\to 1$ and the rank of U becomes lower than the dimension of the space of occupied states. This leads to the vanishing of $\mathrm{Det}(U)$ and crucially forces U^{-1} to acquire very large matrix elements. From

$$\sum_{p_i} p_i^2 = \operatorname{Tr}(\bar{P}^2) = \sum_{m,n \in occ} \langle \psi_m^L | \Gamma_A | \psi_n^R \rangle \langle \psi_n^L | \Gamma_A | \psi_m^R \rangle$$

$$= \sum_{m,n \in occ} (U^{-1} \Gamma_A U)_{mn} (U^{-1} \Gamma_A U)_{nm} \quad (6)$$

where we have used $\Gamma_A^2 = \Gamma_A$, we deduce that at least one of the p_i must also have become very large, since the divergent elements in U^{-1} do not in general cancel off with the small elements in $\Gamma_A U$ except in the case of vanishing entanglement cut $\Gamma_A = I$. However, we stress that even when U is still full-rank with non-defective eigenspace, η can already be extremely close to unity and contribute to negative entanglement.

Negative entanglement from exceptional topological crossing.— In this section and the next, we showcase

two illustrative 2D systems where topologically protected edge states with $\eta \approx 1$ contribute negative entanglement to different degrees of success. We consider a twisted [75] cylindrical geometry such that the y direction contains L_y unit cells, and is bounded so as to host topological edge states. The other translation-invariant (circumferential) direction contains L unit cells, and we shall assign half i.e. L/2 of it to be the entanglement subregion A. P(k) projects onto the occupied lower half bands with $\text{Re}[E(k)] < E_F = 0$ unless otherwise stated. To emphasize the cut direction, we label its unit cells and momentum as L and k instead of L_x and k_x .

First, we showcase a model with two topological edge modes that intersect at an exceptional crossing. Unlike typical topological band crossings [76–82] where the topological modes just have to be energetically degenerate, here we require them to also coalesce i.e. become parallel. A candidate model is given by the following 4-band Hamiltonian [73]

$$\mathcal{H}(k, k_y) = (\cos k_y - \sin k - M)\tau_x \sigma_0 + \tau_y (\cos k\sigma_x - \sigma_y + \sin k_y \sigma_z) + (\sin \alpha \tau_0 + \cos \alpha \tau_x) \sum_{\mu = x, y, z} \sigma_\mu + i\delta \tau_y \sigma_0.$$
 (7)

where the σ_{μ} and τ_{μ} Pauli matrices act in spin and sublattice space respectively. The first term controls the band inversion through M, the second term represents the spin-orbit coupling which break time-reversal, and the third term introduces a Zeeman field that can also involve sublattice hoppings. The final term, $i\delta\tau_y\sigma_0$, introduces non-Hermticity through sublattice hopping asymmetry.

In Fig. 1, we present three distinct scenarios corresponding to different parameter combinations, focusing particularly on the overlap $\eta(k)$ between the middle two eigenstates which straddle the Fermi energy $E_F = 0$ (dashed line). Open boundary conditions (OBCs) are taken only along the y direction, such that k remains a good quantum number. In Fig. 1(a) with intersecting Hermitian topological modes (blue), $\eta(k) = 0$ due to the exact orthonormality of Hermitian eigenstates. In Fig. 1(b) which is non-Hermitian ($\delta \neq 0$), $\eta(k)$ remains essentially zero due to the substantial bulk gap. However, in the non-Hermitian case with topological modes [Fig. 1(c)], the topological edge modes (red) cross and coalesce, forming an exceptional point, as reflected by the saturated squared overlap of $\eta(0) = 1$. Only for this exceptional topological case do we see negatively entanglement entropy S_A [Fig. 1(d)]; for the previous two gapless and gapped cases of Figs. 1(a,b), S_A respectively grows/saturates with L as expected from usual conformal field theory [83–87].

Empirically, the

$$\text{Re}[S_A] \sim -0.3399 \log L \approx \left(\frac{1}{3} - \frac{2}{3}\right) \log L,$$
 (8)

scaling in the exceptional topological case differs from the previously reported $S_A \sim -\frac{2}{3} \log L$ scaling for a linearly dispersive exceptional point [65, 66, 68]. This discrepancy is attributed to gapless non-exceptional gapless crossing [gray in

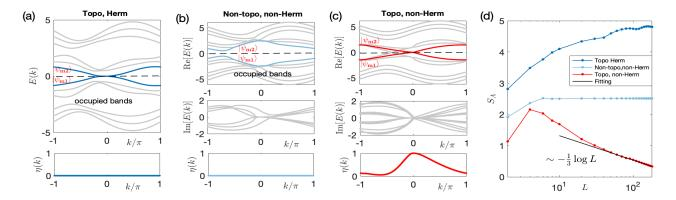


FIG. 1. Negative entanglement in the 4-band exceptional topological crossing model (Eq. (7)) under y-OBCs with $L_y = 3$. (a) In the topologically non-trivial but Hermitian case ($\alpha = 0, M = 1.2, \delta = 0$), the squared overlap $\eta(k)$ [Eq. (5)] of the topological eigenstates (blue) vanishes rigorously. (b) In the topologically trivial (gapped), non-Hermitian case ($\alpha = 0.5\pi, M = 3, \delta = 2$), $\eta(k)$ of the closest bulk states (light blue) still vanishes essentially. (c) For the non-trivial Chern case ($\alpha = 0, M = 3, \delta = 2$), perfect overlap i.e. $\eta(k) = 1$ is reached where topological edge modes (red) cross. (d) The free fermion entanglement entropy S_A (considering only the real part) for cases (a,b) respectively increases and saturates with system circumference L as expected, but that from the topological exceptional crossing (c) exhibits a new $-\frac{1}{3} \log L$ scaling. The entanglement subregion is taken to be the half-cylinder with width L/2.

Fig.1(c)], which contributes the usual $\frac{1}{3} \log L$ entanglement. As such, the negative entanglement from exceptional topological crossings can be easily overshadowed by other non-exceptional topological crossings, and is in this sense not necessarily robust [88].

Enhanced negative entanglement from topological flat bands.— We next showcase an alternative construction that results in far more robust negative entanglement. Departing from the exceptional topological crossing paradigm, the key idea is that the non-Hermitian skin effect (NHSE) localizes all states towards a common boundary, such that the states would exhibit extremely high overlap if they are furthermore macroscopically energetically degenerate, as in a topological flat band. From our results below, this holds true even if the flat bands are not strictly gapless or defective.

To realize topologically protected flat bands across an extended range of k, it suffices to consider a minimal 2-component [89] Hamiltonian

$$H(k, k_y) = \begin{pmatrix} 0 & te^{-ik_y} + a_0 \\ te^{ik_y} + (b_0 - \cos k)^B & 0 \end{pmatrix}, \tag{9}$$

with k-dependent asymmetric off-diagonal hoppings, where a_0, b_0 and hopping distance B > 0 are all real. Under y-direction OBCs, the NHSE results in boundary state localization with a skin depth of $-2/\log[(b_0 - \cos k)^B/a_0]$ and dynamically induces a real energy spectrum from non-Bloch PT-symmetry [90–101]. Almost-flat topological bands exist whenever

$$|a_0(b_0 - \cos k)^B| \le t^2,\tag{10}$$

although they are *not necessarily* gapless for any L_y : Employing Schur's determinant identity on the real-space Hamiltonian $[H_{y\text{-OBC}}(k)]_{y_1,y_2} = (2\pi)^{-1} \int e^{ik_y(y_1-y_2)} H(k,k_y) \, dk_y$, as elaborated in Sect. II.A of the Supplement [73], we have

$$\det[H_{v-OBC}(k)] = [a_0(b_0 - \cos k)^B]^{L_y}, \tag{11}$$

implying that for $0 < |a_0(b_0 - \cos k)^B| < 1$, the topological gap also exhibits a $\Delta \sim (\text{Const.})^{-BL_y}$ inverse exponential scaling to zero as $L_y \to \infty$ (as derived in Sect. II.A of the Supplement [73]), even though it never exactly closes. This implies exponentially dependence of band flatness with BL_y . Perfect gap closure is only possible for $|b_0| \le 1$, and below we investigate these two cases separately.

1. Gapped topological flat bands ($b_0 > 1$). – Even though the topological bands are gapped, they become almost flat and touching as L_y is increased, as depicted in Figs. 2(a,b). At large L_{v} , their gap becomes exponentially small within the topologically non-trivial region given by Eq. (10), where the overlap factor $\eta(k) \approx 1$. This suggests that states within an extensive continuum of k closely approximate EPs, which is unexpected since the Hamiltonian $H(k, k_v)$ in Eq. (9) does not inherently feature EP crossings. As a comparison, for periodic boundary conditions(PBCs) in the y direction [Fig. 2(c)], the topological flat band is absent, and the overlap $\eta(k)$ does not approach 1 even as L_{ν} increased to a large value of 25 where the (bulk) band gap becomes quite narrow. For y-OBCs, even at very small $L_v \approx 5$ number of layers, $\eta(k)$ is already very close to one [Fig. 2(d)]; at larger L_y , $\eta(k)$ converges exponentially to 1 despite the system being physically gapped.

This strong topological flat band-induced nonorthogonality ($\eta \approx 1$) is manifested in a strongly negative bipartite entanglement entropy S_A . As shown in Fig. 2(e), S_A scales negatively with the cylinder circumference $\log L$, with a gradient that grows with its length L_y . From Sect. II.C of the Supplement [73], the exact dependence is established as $S_A \sim -(\alpha L_y + \beta) \log L$, where $\alpha \approx 0.6633$, $\beta \approx -4.1817$ as obtained from numerical fitting. Notably, this linear dependence on L_y does *not* arise trivially because the length of the entanglement cut scales with L_y , since it is contributed only by the topological modes whose number do not scale extensively with system length. Rather, it arises because the

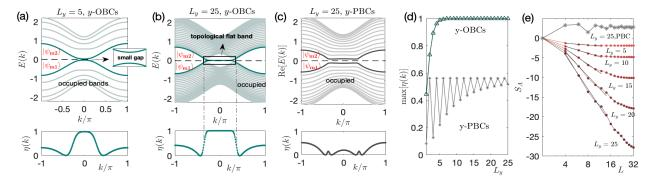


FIG. 2. Robustly negative entanglement entropy from the gapped topological flat bands of our 2-component Hamiltonian (Eq. (9)), for parameters $B=1, t=0.8, a_0=1$ (with $b_0=1.2\neq 1$ to open up the gap). (a) For small cylinder length $L_y=5$ and y-direction OBCs, the energy spectrum E(k) of the topological edge states $|\psi_{m1}\rangle$, $|\psi_{m2}\rangle$ (bolded) exhibits a small but visible gap, but their overlap factor $\eta(k)$ already approaches unity. (b) Upon increasing L_y to 25, a topological flat band with exponentially small gap is observed within the nontrivial regime prescribed by Eq.(10), with $\eta(k)\approx 1$ extremely closely. (c) With y-PBCs, the midgap flat band disappears and $\eta(k)$ deviates markedly from unity, even though the gap is still small. (d) For y-OBCs but not y-PBCs, the overlap $\eta(k)$ saturates very close to unity once $L_y\sim 10^1$. (e) The entanglement entropy scaling behavior S_A for different L_y . Notably, as L_y increases, S_A decreases with log L more rapidly as $S_A\sim -(\alpha L_y+\beta)\log L$, with $\alpha\approx 0.6633$, $\beta\approx -4.1817$ according to obtained from numerical fitting (black). It also saturates at $S_{min}\sim -L_y$ when $L\gtrapprox L_y$.

band flatness scales exponentially with L_y . That said, for a given L_y , the entanglement entropy S_A saturates at negative lower bound [73] $S_{min} \sim -L_y \log[a_0(b_0-1)^{-B}]$ because the system is ultimately gapped, such that the overlap η at $k_0 = \pi/L$ (nearest point to k=0) does not approach arbitrarily close to 1 with increasing L. For PBCs, the bulk gap also results in the saturation of S_A at a positive value, as depicted by the starred grey trend in Fig. 2(e).

2. Gapless topological flat bands ($b_0 = 1$) with super volume-law negative entanglement. – Finally, we discuss the most intriguing case where $\det[H_{y\text{-OBC}}(k)] = 0$ at k = 0 [Eq. (11)], such that the topological band gap vanishes exactly [Fig. 3(a)]. Even though its band structure looks superficially similar to the $b_0 > 1$ case with exponentially small gap [Fig. 2], its entanglement entropy exhibits a surprising super volume-law dependence $S_A \sim -\frac{1}{2}B^2L_y^2\log L$, proportional not to the cylinder length L_y , but to the square of it. While the first power of L_y can be attributed to the exponentially high topological band flatness as before, the additional second power of L_y emerges from an uniquely new 2D phenomenon which we call non-Hermitian critical skin compression (nHCSC).

To understand the nHCSC, recall that all states are pushed to the cylinder's edges due to the *y*-hopping asymmetry in our model Eq. (9). In particular, the left and right biorthogonal topological eigenstates exhibit exponential spatial-*y* profiles $\langle \psi_{edge}^L(k,y)| \sim r(k)^{-y}$ and $|\psi_{edge}^R(k,y)\rangle \sim r(k)^y$ with $r(k) = \sqrt{|(1-\cos k)^B/a_0|} < 1$, and are localized at edges $y = L_y$ and y = 1 respectively. Since these are the two eigenstates that exhibit the highest overlap $\eta(k)$, they dominate the entanglement contribution in \bar{P} . Due to their criticality (gaplessness), r(0) = 0 and the state is perfectly skin-localized for the k = 0 topological mode in the *x*-direction along the cylinder edge.

Ordinarily, this perfect edge localization (or "compression") only leads to irreversible 1D non-Bloch dynamics [102]

and singular generalized Brillouin zones [103–110]. However, in our 2D topological entanglement context, it also causes the occupied band projector

$$[P(k)]_{y,y'} \approx |\psi_{edge}^{R}(k,y)\rangle \langle \psi_{edge}^{L}(k,y')| \sim r(k)^{y-y'}$$
 (12)

to diverge for matrix blocks y < y', with strongest divergence in $[P(k)]_{1,L_y} \sim r(k)^{-L_y} \sim (1-\cos k)^{-BL_y/2}$. Notably, the most strongly divergent contribution $\sim k^{-BL_y}$ from $(1-\cos k)^{-BL_y/2}$ does *not* dominate the total negative entanglement; of also substantial significance are the entire set of divergent terms k^{-BL_y+2} , k^{-BL_y+4} , k^{-BL_y+6} , ... from the sub-leading terms in the expansion of $(1-\cos k)^{-BL_y/2}$, as well as other $[P(k)]_{y,y'}$ [see [73] Sect. II.B]. Consequently, distinct from ordinary EP crossings [65, 66, 73], essentially the *entire* set of \bar{P} eigenvalues p_i diverges with L:

$$p_i \sim \{L^{\frac{BL_y-1}{2}}, L^{\frac{BL_y-1}{2}-1}, L^{\frac{BL_y-1}{2}-2}, ...\}$$
 (13)

This is the main consequence of nHCSC, which hinges on both the edge compression of the eigenstates and its criticality (vanishing of r(k)). The hierarchy of these divergent occupancy eigenvalues is shown in Fig. 3(b): upon closer inspection, subdominant $p_2, p_3 \sim L^{\frac{BLy^{-1}}{2}-1}, L^{\frac{BLy^{-1}}{2}-2}$ eigenvalues (green, blue) are observed in addition to the dominant $p_1 \sim L^{\frac{BLy^{-1}}{2}}$. Summing over them, the total entanglement entropy scales like [73]

$$S_{A} = -\sum_{p_{i}} p_{i} \log p_{i} + (1 - p_{i}) \log(1 - p_{i})$$

$$\approx -\left[\frac{BL_{y} - 1}{2} + \left(\frac{BL_{y} - 1}{2} - 1\right) + \left(\frac{BL_{y} - 1}{2} - 2\right) + \dots\right] \log L$$

$$\approx -\frac{1}{2} (BL_{y})^{2} \log L. \tag{14}$$

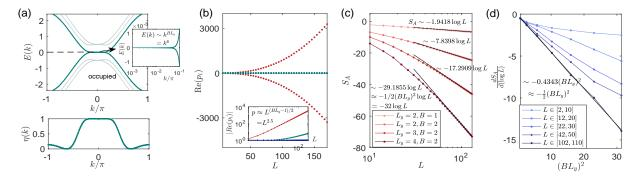


FIG. 3. Very robustly super volume-law negative entanglement entropy S_A from gapless topological flat bands of our 2-component Hamiltonian (Eq. (9)) with parameters $b_0=1, t=0.5, a_0=2$. (a) Even for small $L_y=3, B=2$, a topological gapless flat band (bolded) with dispersion $E_e(k) \sim k^{BL_y}$ and overlap $\eta(k) \approx 1$ emerges around k=0 under y-OBCs. (b) For this gapless case, occupancy eigenvalues p_i (Eq. 13) of \bar{P} dramatically exceed the [0,1] interval due to non-Hermitian critical skin compression (nHCSC), with $p_1, p_2, p_3, ...$ (red, green, blue...) exhibiting a hierarchy of power-law dependencies with L (inset). (c) The negative entanglement scaling is accurately approximated by $S_A \approx -\frac{1}{2}(BL_y)^2 \log L$ (Eq. (14), black) across different B, L_y combinations for sufficiently large cylinder circumference L. This is manifestly super volume-law behavior with respect to the cylinder length L_y . (d) The coefficient of $\log L$ in the numerical S_A , extracted through the gradient of the $dS_A/d(\log L)$ plots (shades of blue), agrees well with $-\frac{1}{2}(BL_y)^2$ (Eq. (14) when $L \geq 10^2$. At smaller L, super volume-law dependence $\propto (BL_y)^2$ still holds for smaller BL_y , albeit with a smaller coefficient.

This strongly negative entanglement S_A is plotted in Fig. 3(c) for various B, L_y , and can be as low as -70 for reasonably large $L_y = 4$, B = 2. By examining the slope of S_A with respect to the universal log L factor, it is numerically confirmed in Fig. 3(d) that the super volume-law quadratic coefficient $-(BL_y)^2/2$ accurately holds for across a wide range of BL_y as long as $L \ge 10^2$ (even though moderately large $L \sim O(10)$ suffices when BL_y is also of O(10)).

Discussion.— We have established that negative free fermion entanglement fundamentally relies on substantial eigenstate overlap around the Fermi surface, which is less stringent than the previously suggested requirement of an exceptional crossing [65]. As such, macroscopically degenerate flatbands resulting from simultaneous topological and non-Hermitian skin localization can lead to strongly negative entanglement entropy, even in the presence of a small gap. Most strikingly, when this gap closes, the system furthermore exhibits super volume-law entanglement scaling $S_A \sim -\frac{1}{2}L_y^2 \log L$, even though the entanglement cut is only of length L_{ν} . This is attributed to a new mechanism known as non-Hermitian critical skin compression (nHCSC), where the criticality of highly degenerate NHSE-compressed topological modes gives rise to an extensive hierarchy of probability non-conserving \bar{P} eigenstates that gives rise to even stronger negative S_A . This negative entanglement also applies to the Rényi entropy which can be physically measured as suggested in [73], placing topology as a potentially practical control knob for probability nonconserving negative entanglement.

Acknowledgments.— We thank Ruizhe Shen and Linhu Li for helpful discussions. This work is supported by the National Research Foundation, Singapore under its QEP2.0 programme (NRF2021-QEP2-02-P09) as well as the Ministry of Education, Singapore (MOE award number: MOE-T2EP50222-0003).

- D. Gioev and I. Klich, Entanglement entropy of fermions in any dimension and the widom conjecture, Phys. Rev. Lett. 96, 100503 (2006).
- [2] S. T. Flammia, A. Hamma, T. L. Hughes, and X.-G. Wen, Topological entanglement rényi entropy and reduced density matrix structure, Phys. Rev. Lett. 103, 261601 (2009).
- [3] M. Srednicki, Entropy and area, Phys. Rev. Lett. 71, 666 (1993).
- [4] J. Eisert, M. Cramer, and M. B. Plenio, Colloquium: Area laws for the entanglement entropy, Rev. Mod. Phys. **82**, 277 (2010).
- [5] A. Kitaev and J. Preskill, Topological entanglement entropy, Phys. Rev. Lett. 96, 110404 (2006).
- [6] H. Li and F. D. M. Haldane, Entanglement spectrum as a generalization of entanglement entropy: Identification of topological order in non-abelian fractional quantum hall effect states, Phys. Rev. Lett. 101, 010504 (2008).
- [7] M. Levin and X.-G. Wen, Detecting topological order in a ground state wave function, Phys. Rev. Lett. 96, 110405 (2006).
- [8] G. Vidal, J. I. Latorre, E. Rico, and A. Kitaev, Entanglement in quantum critical phenomena, Phys. Rev. Lett. 90, 227902 (2003).
- [9] A. Hamma, R. Ionicioiu, and P. Zanardi, Ground state entanglement and geometric entropy in the kitaev model, Physics Letters A 337, 22 (2005).
- [10] J. Cho and K. W. Kim, Quantum phase transition and entanglement in topological quantum wires, Scientific Reports 7, 2745 (2017).
- [11] S. Yao, F. Song, and Z. Wang, Non-hermitian chern bands, Phys. Rev. Lett. 121, 136802 (2018).
- [12] C. H. Lee and R. Thomale, Anatomy of skin modes and topology in non-hermitian systems, Phys. Rev. B 99, 201103 (2019).
- [13] F. Song, S. Yao, and Z. Wang, Non-hermitian topological invariants in real space, Phys. Rev. Lett. 123, 246801 (2019).
- [14] F. Song, S. Yao, and Z. Wang, Non-hermitian skin effect and

- chiral damping in open quantum systems, Phys. Rev. Lett. 123, 170401 (2019).
- [15] R. Lin, T. Tai, L. Li, and C. H. Lee, Topological non-hermitian skin effect, Frontiers of Physics 18, 53605 (2023).
- [16] K. Kawabata, K. Shiozaki, and M. Ueda, Anomalous helical edge states in a non-hermitian chern insulator, Phys. Rev. B 98, 165148 (2018).
- [17] S. Longhi, Probing non-hermitian skin effect and non-bloch phase transitions, Phys. Rev. Res. 1, 023013 (2019).
- [18] H. Jiang, L.-J. Lang, C. Yang, S.-L. Zhu, and S. Chen, Interplay of non-hermitian skin effects and anderson localization in nonreciprocal quasiperiodic lattices, Phys. Rev. B 100, 054301 (2019).
- [19] K. Zhang, Z. Yang, and C. Fang, Correspondence between winding numbers and skin modes in non-hermitian systems, Phys. Rev. Lett. 125, 126402 (2020).
- [20] K. Yokomizo and S. Murakami, Non-bloch band theory of non-hermitian systems, Phys. Rev. Lett. 123, 066404 (2019).
- [21] K. Kawabata, K. Shiozaki, M. Ueda, and M. Sato, Symmetry and topology in non-hermitian physics, Phys. Rev. X 9, 041015 (2019).
- [22] K. Kawabata, M. Sato, and K. Shiozaki, Higher-order nonhermitian skin effect, Physical Review B 102, 205118 (2020).
- [23] Z. Yang, K. Zhang, C. Fang, and J. Hu, Non-hermitian bulk-boundary correspondence and auxiliary generalized brillouin zone theory, Phys. Rev. Lett. 125, 226402 (2020).
- [24] D. S. Borgnia, A. J. Kruchkov, and R.-J. Slager, Non-hermitian boundary modes and topology, Physical review letters 124, 056802 (2020).
- [25] F. Qin, Y. Ma, R. Shen, and C. H. Lee, Universal competitive spectral scaling from the critical non-hermitian skin effect, Phys. Rev. B 107, 155430 (2023).
- [26] L. Li, S. Mu, C. H. Lee, and J. Gong, Quantized classical response from spectral winding topology, Nature Communications 12, 5294 (2021).
- [27] X.-Q. Sun, P. Zhu, and T. L. Hughes, Geometric response and disclination-induced skin effects in non-hermitian systems, Phys. Rev. Lett. 127, 066401 (2021).
- [28] R. Yang, J. W. Tan, T. Tai, J. M. Koh, L. Li, S. Longhi, and C. H. Lee, Designing non-hermitian real spectra through electrostatics, Science Bulletin 67, 1865 (2022).
- [29] K. Zhang, Z. Yang, and C. Fang, Universal non-hermitian skin effect in two and higher dimensions, Nature Communications 13, 2496 (2022).
- [30] R. Shen and C. H. Lee, Non-hermitian skin clusters from strong interactions, Communications Physics 5, 238 (2022).
- [31] L. Li and C. H. Lee, Non-hermitian pseudo-gaps, Science Bulletin 67, 685 (2022).
- [32] C.-A. Li, B. Trauzettel, T. Neupert, and S.-B. Zhang, Enhancement of second-order non-hermitian skin effect by magnetic fields, Physical Review Letters 131, 116601 (2023).
- [33] H. Jiang and C. H. Lee, Dimensional transmutation from nonhermiticity, Physical Review Letters 131, 076401 (2023).
- [34] K. Cao, Q. Du, and S.-P. Kou, Many-body non-hermitian skin effect at finite temperatures, Physical Review B 108, 165420 (2023).
- [35] S. Ke, W. Wen, D. Zhao, and Y. Wang, Floquet engineering of the non-hermitian skin effect in photonic waveguide arrays, Physical Review A 107, 053508 (2023).
- [36] T. Tai and C. H. Lee, Zoology of non-hermitian spectra and their graph topology, Phys. Rev. B 107, L220301 (2023).
- [37] Z. Li, L.-W. Wang, X. Wang, Z.-K. Lin, G. Ma, and J.-H. Jiang, Observation of dynamic non-hermitian skin effects, arXiv preprint arXiv:2312.07564 (2023).

- [38] R. Shen, T. Chen, B. Yang, and C. H. Lee, Observation of the non-hermitian skin effect and fermi skin on a digital quantum computer (2023), arXiv:2311.10143 [quant-ph].
- [39] N. Okuma and M. Sato, Non-hermitian topological phenomena: A review, Annual Review of Condensed Matter Physics 14, 83 (2023).
- [40] G.-G. Liu, S. Mandal, P. Zhou, X. Xi, R. Banerjee, Y.-H. Hu, M. Wei, M. Wang, Q. Wang, Z. Gao, *et al.*, Localization of chiral edge states by the non-hermitian skin effect, Physical Review Letters 132, 113802 (2024).
- [41] Z. Lei, C. H. Lee, and L. Li, Activating non-hermitian skin modes by parity-time symmetry breaking, Communications Physics 7, 100 (2024).
- [42] G. Lee, A. McDonald, and A. Clerk, Anomalously large relaxation times in dissipative lattice models beyond the nonhermitian skin effect, Physical Review B 108, 064311 (2023).
- [43] H. Hu, Non-hermitian band theory in all dimensions: uniform spectra and skin effect, arXiv preprint arXiv:2306.12022 (2023).
- [44] R. Shen, T. Chen, M. M. Aliyu, F. Qin, Y. Zhong, H. Loh, and C. H. Lee, Proposal for observing yang-lee criticality in rydberg atomic arrays, Physical Review Letters 131, 080403 (2023).
- [45] Y.-C. Wang, K. Suthar, H. Jen, Y.-T. Hsu, and J.-S. You, Non-hermitian skin effects on thermal and many-body localized phases, Physical Review B 107, L220205 (2023).
- [46] Q. Zhou, J. Wu, Z. Pu, J. Lu, X. Huang, W. Deng, M. Ke, and Z. Liu, Observation of geometry-dependent skin effect in nonhermitian phononic crystals with exceptional points, Nature Communications 14, 4569 (2023).
- [47] R. Shen, F. Qin, J.-Y. Desaules, Z. Papić, and C. H. Lee, Enhanced many-body quantum scars from the non-hermitian fock skin effect (2024), arXiv:2403.02395 [cond-mat.quantgas].
- [48] Y. Qin, C. H. Lee, and L. Li, Dynamical suppression of manybody non-hermitian skin effect in anyonic systems (2024), arXiv:2405.12288 [quant-ph].
- [49] H.-Y. Wang, F. Song, and Z. Wang, Amoeba formulation of non-bloch band theory in arbitrary dimensions, Phys. Rev. X 14, 021011 (2024).
- [50] H. Meng, Y. S. Ang, and C. H. Lee, Exceptional points in non-hermitian systems: Applications and recent developments, Applied Physics Letters 124 (2024).
- [51] S. Longhi, Incoherent non-hermitian skin effect in photonic quantum walks, Light: Science & Applications 13, 95 (2024).
- [52] K. Zhang, Z. Yang, and K. Sun, Edge theory of non-hermitian skin modes in higher dimensions, Physical Review B 109, 165127 (2024).
- [53] Y. Xiong, Z.-Y. Xing, and H. Hu, Non-hermitian skin effect in arbitrary dimensions: non-bloch band theory and classification, arXiv preprint arXiv:2407.01296 (2024).
- [54] D. C. Brody, Biorthogonal quantum mechanics, Journal of Physics A: Mathematical and Theoretical 47, 035305 (2013).
- [55] S. Weigert, Completeness and orthonormality in PTsymmetric quantum systems, Phys. Rev. A 68, 062111 (2003).
- [56] F. K. Kunst, E. Edvardsson, J. C. Budich, and E. J. Bergholtz, Biorthogonal bulk-boundary correspondence in non-hermitian systems, Phys. Rev. Lett. 121, 026808 (2018).
- [57] P. T. Leung, W. M. Suen, C. pu Sun, and K. R. Young, Waves in open systems via a biorthogonal basis, Physical Review E 57, 6101 (1998).
- [58] C. M. Bender and S. Boettcher, Real spectra in non-hermitian hamiltonians having PT symmetry, Phys. Rev. Lett. 80, 5243 (1998).

- [59] M. V. Berry, Physics of nonhermitian degeneracies, Czechoslovak Journal of Physics 54, 1039 (2004).
- [60] Z. Gong, Y. Ashida, K. Kawabata, K. Takasan, S. Hi-gashikawa, and M. Ueda, Topological phases of non-hermitian systems, Phys. Rev. X 8, 031079 (2018).
- [61] N. Moiseyev, Non-Hermitian Quantum Mechanics (Cambridge University Press, 2011).
- [62] I. Rotter, A non-hermitian hamilton operator and the physics of open quantum systems, Journal of Physics A: Mathematical and Theoretical 42, 153001 (2009).
- [63] N. J. Cerf and C. Adami, Negative entropy and information in quantum mechanics, Phys. Rev. Lett. 79, 5194 (1997).
- [64] S. Salek, R. Schubert, and K. Wiesner, Negative conditional entropy of postselected states, Phys. Rev. A 90, 022116 (2014).
- [65] P.-Y. Chang, J.-S. You, X. Wen, and S. Ryu, Entanglement spectrum and entropy in topological non-hermitian systems and nonunitary conformal field theory, Phys. Rev. Res. 2, 033069 (2020).
- [66] C. H. Lee, Exceptional bound states and negative entanglement entropy, Phys. Rev. Lett. 128, 010402 (2022).
- [67] D. Zou, T. Chen, H. Meng, Y. S. Ang, X. Zhang, and C. H. Lee, Experimental observation of exceptional bound states in a classical circuit network, Science Bulletin 69, 2194 (2024).
- [68] Y.-T. Tu, Y.-C. Tzeng, and P.-Y. Chang, Rényi entropies and negative central charges in non-Hermitian quantum systems, SciPost Phys. 12, 194 (2022).
- [69] M. Fossati, F. Ares, and P. Calabrese, Symmetry-resolved entanglement in critical non-hermitian systems, Physical Review B 107, 205153 (2023).
- [70] F. Rottoli, M. Fossati, and P. Calabrese, Entanglement hamiltonian in the non-hermitian ssh model, Journal of Statistical Mechanics: Theory and Experiment 2024, 063102 (2024).
- [71] I. Peschel, Calculation of reduced density matrices from correlation functions, Journal of Physics A: Mathematical and General 36, L205 (2003).
- [72] An analogous expression also holds for free bosons: $S_{A,boson}^{(n)} = \frac{1}{n-1} \text{Tr} \Big[\log \Big(\bar{P}^n (\bar{P} I)^n \Big) \Big].$
- [73] Supplemental material for "topologically protected negative entanglement" (2024).
- [74] η can be viewed as a variant of the Petermann factor [111–118].
- [75] Such that the discrete momentum takes values of $k = \pi/L$, $3\pi/L$, ..., avoiding the singular k = 0 point exactly.
- [76] M. Z. Hasan and C. L. Kane, Colloquium: Topological insulators, Rev. Mod. Phys. **82**, 3045 (2010).
- [77] N. P. Armitage, E. J. Mele, and A. Vishwanath, Weyl and dirac semimetals in three-dimensional solids, Rev. Mod. Phys. 90, 015001 (2018).
- [78] S. M. Young, S. Zaheer, J. C. Y. Teo, C. L. Kane, E. J. Mele, and A. M. Rappe, Dirac semimetal in three dimensions, Phys. Rev. Lett. 108, 140405 (2012).
- [79] C. H. Lee and X.-L. Qi, Lattice construction of pseudopotential hamiltonians for fractional chern insulators, Physical Review B 90, 085103 (2014).
- [80] H. Weng, C. Fang, Z. Fang, B. A. Bernevig, and X. Dai, Weyl semimetal phase in noncentrosymmetric transitionmetal monophosphides, Phys. Rev. X 5, 011029 (2015).
- [81] W. Chen and A. P. Schnyder, Universality classes of topological phase transitions with higher-order band crossing, New Journal of Physics 21, 073003 (2019).
- [82] K. Yang, Z. Li, J. L. K. König, L. Rødland, M. Stålhammar, and E. J. Bergholtz, Homotopy, symmetry, and non-hermitian

- band topology, Reports on Progress in Physics 87, 078002 (2024).
- [83] C. Callan and F. Wilczek, On geometric entropy, Physics Letters B 333, 55 (1994).
- [84] T. M. Fiola, J. Preskill, A. Strominger, and S. P. Trivedi, Black hole thermodynamics and information loss in two dimensions, Phys. Rev. D 50, 3987 (1994).
- [85] C. Holzhey, F. Larsen, and F. Wilczek, Geometric and renormalized entropy in conformal field theory, Nuclear Physics B 424, 443 (1994).
- [86] S. Hawking, J. Maldacena, and A. Strominger, Desitter entropy, quantum entanglement and ads/cft, Journal of High Energy Physics 2001, 001 (2001).
- [87] P. Calabrese and J. Cardy, Entanglement entropy and quantum field theory, Journal of Statistical Mechanics: Theory and Experiment 2004, P06002 (2004).
- [88] This is particularly so if the exceptional dispersion is squareroot, as for some generalizations of our model [73].
- [89] 2 topological bands are sufficient, since the NHSE pushes both of them onto the same boundary and makes them overlap significantly.
- [90] C. M. Bender, M. V. Berry, and A. Mandilara, Generalized pt symmetry and real spectra, Journal of Physics A: Mathematical and General 35, L467 (2002).
- [91] C. M. Bender, Making sense of non-hermitian hamiltonians, Reports on Progress in Physics 70, 947 (2007).
- [92] H. Hodaei, M. A. Miri, A. U. Hassan, W. E. Hayenga, M. Heinrich, D. N. Christodoulides, and M. Khajavikhan, Parity-time-symmetric coupled microring lasers operating around an exceptional point, Opt. Lett. 40, 4955 (2015).
- [931 L. Z. J. Wong, R.-M. Ma, Feng, Y. Wang. parity-time by and X. Zhang, Single-mode laser symmetry breaking. Science 346. 972 (2014).https://www.science.org/doi/pdf/10.1126/science.1258479.
- [94] S. Yao and Z. Wang, Edge states and topological invariants of non-hermitian systems, Phys. Rev. Lett. 121, 086803 (2018).
- [95] Z. Lei, C. H. Lee, and L. Li, PT-activated non-hermitian skin modes (2023), arXiv:2304.13955 [cond-mat.mes-hall].
- [96] R. El-Ganainy, K. G. Makris, M. Khajavikhan, Z. H. Musslimani, S. Rotter, and D. N. Christodoulides, Non-hermitian physics and pt symmetry, Nature Physics 14, 11 (2018).
- [97] Ş. K. Özdemir, S. Rotter, F. Nori, and L. Yang, Parity-time symmetry and exceptional points in photonics, Nature Materials 18, 783 (2019).
- [98] C. E. Rüter, K. G. Makris, R. El-Ganainy, D. N. Christodoulides, M. Segev, and D. Kip, Observation of parity time symmetry in optics, Nature Physics 6, 192 (2010).
- [99] B. Zhang, Q. Li, X. Zhang, and C. H. Lee, Real non-hermitian energy spectra without any symmetry, Chinese Physics B 31, 070308 (2022).
- [100] M.-H. L. Xiujuan Zhang, Tian Zhang and Y.-F. Chen, A review on non-hermitian skin effect, Advances in Physics: X 7, 2109431 (2022), https://doi.org/10.1080/23746149.2022.2109431.
- [101] M. Yang and C. H. Lee, Percolation-induced pt symmetry breaking, arXiv preprint arXiv:2309.15008 (2023).
- [102] S. Longhi, Non-bloch-band collapse and chiral zener tunneling, Phys. Rev. Lett. 124, 066602 (2020).
- [103] V. M. Martinez Alvarez, J. E. Barrios Vargas, and L. E. F. Foa Torres, Non-hermitian robust edge states in one dimension: Anomalous localization and eigenspace condensation at exceptional points, Phys. Rev. B 97, 121401 (2018).
- [104] L. Pan, S. Chen, and X. Cui, Interacting non-hermitian ultracold atoms in a harmonic trap: Two-body exact solution and a

- high-order exceptional point, Phys. Rev. A 99, 063616 (2019).
- [105] I. Mandal and E. J. Bergholtz, Symmetry and higher-order exceptional points, Phys. Rev. Lett. 127, 186601 (2021).
- [106] M. Stålhammar and E. J. Bergholtz, Classification of exceptional nodal topologies protected by PT symmetry, Phys. Rev. B 104, L201104 (2021).
- [107] G.-F. Guo, X.-X. Bao, and L. Tan, Non-hermitian bulk-boundary correspondence and singular behaviors of generalized brillouin zone, New Journal of Physics 23, 123007 (2021).
- [108] M. M. Denner, T. Neupert, and F. Schindler, Infernal and exceptional edge modes: non-hermitian topology beyond the skin effect, Journal of Physics: Materials 6, 045006 (2023).
- [109] H. Hodaei, A. U. Hassan, S. Wittek, H. Garcia-Gracia, R. El-Ganainy, D. N. Christodoulides, and M. Khajavikhan, Enhanced sensitivity at higher-order exceptional points, Nature 548, 187 (2017).
- [110] S. Longhi, Non-bloch pt symmetry breaking in non-hermitian photonic quantum walks, Opt. Lett. 44, 5804 (2019).
- [111] K. Petermann, Calculated spontaneous emission factor for double-heterostructure injection lasers with gain-induced waveguiding, IEEE Journal of Quantum Electronics 15, 566 (1979).
- [112] J. T. Chalker and B. Mehlig, Eigenvector statistics in non-hermitian random matrix ensembles, Phys. Rev. Lett. 81, 3367 (1998).
- [113] M. Patra, H. Schomerus, and C. W. J. Beenakker, Quantum-limited linewidth of a chaotic laser cavity, Phys. Rev. A 61, 023810 (2000).
- [114] W. A. Hamel and J. P. Woerdman, Observation of enhanced fundamental linewidth of a laser due to nonorthogonality of its longitudinal eigenmodes, Phys. Rev. Lett. 64, 1506 (1990).
- [115] M. Berry, Mode degeneracies and the peterman excess-noise factor for unstable lasers, Journal of Modern Optics 50 No 1, 63 (2003).
- [116] H. Wang, Y.-H. Lai, Z. Yuan, M.-G. Suh, and K. Vahala, Petermann-factor sensitivity limit near an exceptional point in a brillouin ring laser gyroscope, Nature Communications 11, 1610 (2020)
- [117] Y.-Y. Zou, Y. Zhou, L.-M. Chen, and P. Ye, Detecting bulk and edge exceptional points in non-hermitian systems through generalized petermann factors, Frontiers of Physics 19, 23201 (2023).
- [118] M. C. Zheng, D. N. Christodoulides, R. Fleischmann, and T. Kottos, PT optical lattices and universality in beam dynamics, Phys. Rev. A 82, 010103 (2010).
- [119] M. M. Denner, A. Skurativska, F. Schindler, M. H. Fischer, R. Thomale, T. Bzdušek, and T. Neupert, Exceptional topological insulators, Nature Communications 12, 5681 (2021).
- [120] F. Zhang, The schur complement and its applications (2005).
- [121] C. H. Lee, L. Li, R. Thomale, and J. Gong, Unraveling non-hermitian pumping: Emergent spectral singularities and anomalous responses, Phys. Rev. B 102, 085151 (2020).
- [122] R. Islam, R. Ma, P. M. Preiss, M. Eric Tai, A. Lukin, M. Rispoli, and M. Greiner, Measuring entanglement entropy in a quantum many-body system, Nature 528, 77 (2015).
- [123] A. J. Daley, H. Pichler, J. Schachenmayer, and P. Zoller, Measuring entanglement growth in quench dynamics of bosons in an optical lattice, Phys. Rev. Lett. 109, 020505 (2012).
- [124] X. Zhou, Z. Y. Meng, Y. Qi, and Y. Da Liao, Incremental swap operator for entanglement entropy: Application for exponential observables in quantum monte carlo simulation, Phys. Rev. B 109, 165106 (2024).
- [125] M. B. Hastings, I. González, A. B. Kallin, and R. G. Melko,

- Measuring renyi entanglement entropy in quantum monte carlo simulations, Phys. Rev. Lett. **104**, 157201 (2010).
- [126] J. McMinis and N. M. Tubman, Renyi entropy of the interacting fermi liquid, Phys. Rev. B 87, 081108 (2013).
- [127] A. K. Ekert, C. M. Alves, D. K. L. Oi, M. Horodecki, P. Horodecki, and L. C. Kwek, Direct estimations of linear and nonlinear functionals of a quantum state, Phys. Rev. Lett. 88, 217901 (2002).
- [128] H. Pichler, L. Bonnes, A. J. Daley, A. M. Läuchli, and P. Zoller, Thermal versus entanglement entropy: a measurement protocol for fermionic atoms with a quantum gas microscope, New Journal of Physics 15, 063003 (2013).
- [129] H. Buhrman, R. Cleve, J. Watrous, and R. de Wolf, Quantum fingerprinting, Phys. Rev. Lett. 87, 167902 (2001).
- [130] N. M. Linke, S. Johri, C. Figgatt, K. A. Landsman, A. Y. Matsuura, and C. Monroe, Measuring the rényi entropy of a two-site fermi-hubbard model on a trapped ion quantum computer, Phys. Rev. A 98, 052334 (2018).
- [131] Q. Wang, J. Guan, J. Liu, Z. Zhang, and M. Ying, New quantum algorithms for computing quantum entropies and distances, IEEE Transactions on Information Theory 70, 5653–5680 (2024).
- [132] H.-C. Chang, H.-C. Hsu, and Y.-C. Lin, Probing entanglement dynamics and topological transitions on noisy intermediatescale quantum computers (2024), arXiv:2406.10159 [quantph].
- [133] M. A. Nielsen and I. L. Chuang, Quantum Computation and Quantum Information: 10th Anniversary Edition (Cambridge University Press, 2010).
- [134] S.-H. Lin, R. Dilip, A. G. Green, A. Smith, and F. Pollmann, Real-and imaginary-time evolution with compressed quantum circuits, PRX Quantum 2, 010342 (2021).
- [135] T. Chen, R. Shen, C. H. Lee, and B. Yang, High-fidelity realization of the aklt state on a nisq-era quantum processor, Sci-Post Physics 15, 170 (2023).
- [136] H. H. S. Chan, D. M. Ramo, and N. Fitzpatrick, Simulating non-unitary dynamics using quantum signal processing with unitary block encoding, arXiv preprint arXiv:2303.06161 (2023).
- [137] H. Häffner, W. Hänsel, C. F. Roos, J. Benhelm, D. Chek-al kar, M. Chwalla, T. Körber, U. D. Rapol, M. Riebe, P. O. Schmidt, C. Becher, O. Gühne, W. Dür, and R. Blatt, Scalable multiparticle entanglement of trapped ions, Nature 438, 643 (2005).
- [138] G. Torlai, G. Mazzola, J. Carrasquilla, M. Troyer, R. Melko, and G. Carleo, Neural-network quantum state tomography, Nature Physics 14, 447 (2018).
- [139] C. Kokail, R. van Bijnen, A. Elben, B. Vermersch, and P. Zoller, Entanglement hamiltonian tomography in quantum simulation, Nature Physics 17, 936 (2021).
- [140] J. Zhao, Y.-C. Wang, Z. Yan, M. Cheng, and Z. Y. Meng, Scaling of entanglement entropy at deconfined quantum criticality, Phys. Rev. Lett. 128, 010601 (2022).
- [141] J. Zhao, B.-B. Chen, Y.-C. Wang, Z. Yan, M. Cheng, and Z. Y. Meng, Measuring rényi entanglement entropy with high efficiency and precision in quantum monte carlo simulations, npj Quantum Materials 7, 69 (2022).
- [142] I. Bloch, J. Dalibard, and W. Zwerger, Many-body physics with ultracold gases, Rev. Mod. Phys. 80, 885 (2008).
- [143] I. Bloch, J. Dalibard, and S. Nascimbène, Quantum simulations with ultracold quantum gases, Nature Physics 8, 267 (2012).
- [144] N. Goldman, J. C. Budich, and P. Zoller, Topological quantum matter with ultracold gases in optical lattices, Nature Physics 12, 639 (2016).

- [145] A. Aspuru-Guzik and P. Walther, Photonic quantum simulators, Nature Physics 8, 285 (2012).
- [146] J. Li, A. K. Harter, J. Liu, L. de Melo, Y. N. Joglekar, and L. Luo, Observation of parity-time symmetry breaking transitions in a dissipative floquet system of ultracold atoms, Nature Communications 10, 855 (2019).
- [147] Z. Ren, D. Liu, E. Zhao, C. He, K. K. Pak, J. Li, and G.-B. Jo, Chiral control of quantum states in non-hermitian spin-orbitcoupled fermions, Nature Physics 18, 385 (2022).
- [148] W. Gou, T. Chen, D. Xie, T. Xiao, T.-S. Deng, B. Gadway, W. Yi, and B. Yan, Tunable nonreciprocal quantum transport through a dissipative aharonov-bohm ring in ultracold atoms, Phys. Rev. Lett. 124, 070402 (2020).

Supplemental information for "Topologically protected negative entanglement"

This supplement contains the following material arranged by sections:

- 1. Detailed analysis of the different possible dispersions of the topological edge bands in a generalized 4-band exceptional topological model.
- 2. Analysis of the various scaling properties of the entanglement entropy S_A in the topological flat band model, for both gapless and gapped cases.
- 3. How negativity of the entanglement entropy implies negative Rényi entropy, and constraints on the entanglement spectrum from symmetry.
- 4. A scheme for measuring negative entanglement through the second Rényi entropy.

I. DETAILED ANALYSIS OF THE 4-BAND EXCEPTIONAL TOPOLOGICAL MODEL

A. General form of the Hamiltonian and the EP in its bulk bands

Here, we show how the 4-band exceptional topological model given by Eq. (7) of the main text belongs to a more general family of extended exceptional topological models that exists three dimensions. A possible extension is [119]:

$$H(\mathbf{k}) = \left(\sum_{j=x,y,z} \cos k_j - M\right) \tau_z \sigma_0 + \lambda \sum_{j=x,y,z} \sin k_j \tau_x \sigma_j + [\sin \alpha \tau_0 + \cos \alpha \tau_z] (\vec{Z} \cdot \sigma) + i \delta \tau_x \sigma_0$$
 (S1)

where λ represents the strength of spin-orbit coupling, and $\vec{Z} = (Z, Z, Z)^T$ is the Zeeman field of magnitude $\sqrt{3}Z$ in the (1, 1, 1) direction. Upon the substitution $k_y = -k_0$ with $k_0 = \arcsin(Z)$, and relabeling k_x as k, the above reduces to

$$\mathcal{H}(k, k_z) = (\cos k + \cos k_0 + \cos k_z - M)\tau_z\sigma_0 + \lambda(\sin k\tau_x\sigma_x + \sin(-k_0)\tau_x\sigma_y + \sin k_z\tau_x\sigma_z)$$

$$+ (\sin \alpha\tau_0 + \cos \alpha\tau_z)\vec{Z} \cdot \vec{\sigma} + i\delta\tau_x\sigma_0,$$
(S2)

To simplify the notation, we further relabel k_z as k_y , apply a rotation to the Pauli matrices as $\tau_x \to \tau_y \to \tau_z \to \tau_x$ and shift the spectrum by substituting $k \to k + k_0$, yielding the Hamiltonian:

$$H(k, k_y) = (\cos(k + k_0) + \cos k_0 + \cos k_y - M)\tau_x\sigma_0 + \lambda(\sin(k + k_0)\tau_y\sigma_x + \sin(-k_0)\tau_y\sigma_y + \sin k_y\tau_y\sigma_z)$$

$$+ (\sin\alpha\tau_0 + \cos\alpha\tau_x)\vec{Z}\cdot\vec{\sigma} + i\delta\tau_y\sigma_0.$$
(S3)

Our model in Eq. (7) of the main text can be viewed as a specific instance of this generalized model that possesses the minimal ingredients of exceptional gapless topological modes, characterized by the parameters $\lambda = 1, Z = 1$, and $k_0 = \arcsin(Z) = \pi/2$.

Effect of EP dispersion on entanglement scaling

In Figs. S1 and S2, we aim to demonstrate that the presence of an exceptional points (EP), whether topologically protected or not, does not necessarily imply the occurrence of a negative EE; the outcome also depends on the energy dispersion around the EP. In Fig. S1(a,b), we present a topologically non-trivial configuration, characterized by blue lines that represent the topological edge states for only OBCs and not PBCs. As contrasted with the linear dispersion around the EP discussed in the main text, this scenario exhibits a square-root dispersion, $E_e(k) \sim \sqrt{\delta k}$.

Correspondingly, the overlap factor $\eta(k) = |\langle \psi_m^R | \psi_n^R \rangle|^2/[\langle \psi_m^R(k) | \psi_m^R(k) \rangle \langle \psi_n^R(k) | \psi_n^R(k)]\rangle$ between the two topological states indexed by m,n diminishes rapidly away from the EP k=0. It should be noted that in a tight-binding model, the momentum k is discretized, with $k_1 = \pi/L$ serving as the closest approximation to k=0. Given the rapid decay of $\eta(k)$ around k=0, it follows that $\eta(k_1)$ does not approach 1. Consequently, as observed in Fig. S2(a), \bar{P} exhibits only short-range hoppings, with its eigenvalues p_i almost all located within the range [0,1] (Fig. S2(b)) just like for an ordinary non-exceptional model (other than the fact that p_i possess imaginary parts). Furthermore, the entanglement entropy remains positive and increases steadily with system size L, as shown in Fig. S2(c). Evidently, this scenario with $E_e(k) \sim \sqrt{\delta k}$ dispersion does not exhibit negative entanglement, suggesting that the dispersion around the EP crucially affects whether the entanglement entropy becomes negative. We will elaborate on how this dispersion can be tuned in our model in subsection I.B.

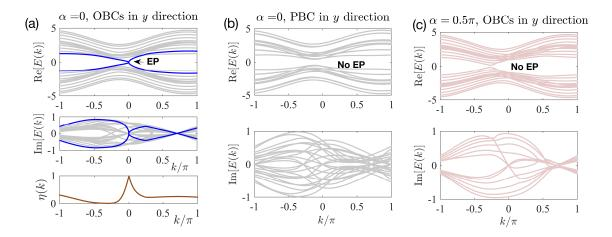


FIG. S1. Parameter and boundary dependence of EPs in our 4-band model given by Eq. (7) of the main text. (a) For $\alpha = 0$ and OBCs in the *y* direction, an EP occurs at k = 0. (b) With PBC in the *y* direction, no EP is observed, implying that the EP arises due to boundary localization. (c) For $\alpha = \pi/2$ with OBCs in the *y* direction, no EP exists either. Other parameters: $L_y = 6$, M = 3, Z = 0.44, $\lambda = \delta = 1$.

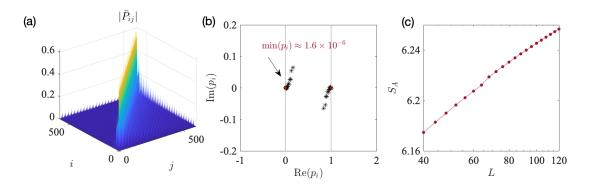


FIG. S2. Absence of (a) divergent truncated projector \bar{P} matrix elements and (b) eigenvalues outside of [0, 1] for an EP with square-root singularities. (c) Consequently, the real part of the entanglement entropy S_A does not exhibit any negativity. Parameters and model are the same as in Fig.S1(a), with x-direction size L = 50 and $L_y = 6$.

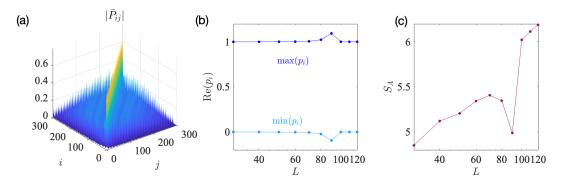


FIG. S3. Slight negative dip in the entanglement entropy due to bulk EPs. Shown is the model in Eq. (7) of the main text, with the Fermi Surface fixed at $E_F = -1.1$ and parameters $L_y = 3$, M = 3 and $\delta = 2$. (a) The truncated projector \bar{P} matrix elements for L = 50 with truncation at l = L/2 = 25. (b) The scaling of the maximum and minimum p_i with system size L, which goes out of the [0, 1] interval only around L = 90. (c) The entanglement entropy S_A hence exhibits a slight negative dip at $L \approx 90$. However, this negative dip from the bulk EP is too weak to cause the entanglement to scale negatively as a whole.

Returning to our model in Eq. (7) of the main text, we noted that EPs also exist in the bulk bands around $Re[E(k)] \approx \pm 1.1$. To investigate whether these bulk EPs could similarly induce a negative-valued entanglement entropy, we adjusted the Fermi energy to align with a bulk EP, setting E_F to 1.1. Observations from Fig.S3(a) indicate that the matrix elements of \bar{P} remain minimal, with p_i going beyond [0, 1] interval only around L = 90 (see Figs.S3(b)). Consequently, the entanglement entropy exhibits a dip at this system size, albeit only a small dip. This occurs because the bulk EP is located at $k' \approx 0.0106\pi$, rather than at the long-wavelength limit k = 0. As L increases, $k_1 = \pi/L$ will pass through the EP k', inducing a dip in S_A . However, S_A generally remains positive and continues to increase with increasing L, indicating that the negative scaling observed in Fig. 1(d) of the main text must be predominantly a consequence of the EP in the topological edge bands crossing at k = 0, rather than of those within the bulk bands.

B. Deriving two types of dispersion relations (linear and square-root) for topological edge bands

For the general form of the Hamiltonian $H(k, k_y)$ as defined in Eq. (S3), when considering OBCs in the y-direction with size L_y , we obtain:

$$H_{y\text{-OBC}}(k) = \begin{pmatrix} h_0^y & h_+^y & \cdots & 0 & 0 \\ h_-^y & h_0^y & h_+^y & \cdots & 0 \\ 0 & h_-^y & h_0^y & \cdots & 0 \\ \vdots & \vdots & \ddots & \ddots & \vdots \\ 0 & 0 & \cdots & h_-^y & h_0^y \end{pmatrix}_{L_v \times L_v}, \text{ with } h_+^y = \begin{pmatrix} 0 & 0 & 0 & 0 \\ 0 & 0 & 0 & 1 \\ 1 & 0 & 0 & 0 \\ 0 & 0 & 0 & 0 \end{pmatrix}, \quad h_-^y = \begin{pmatrix} 0 & 0 & 1 & 0 \\ 0 & 0 & 0 & 0 \\ 0 & 0 & 0 & 0 \\ 0 & 1 & 0 & 0 \end{pmatrix}, \text{ and } h_0^y(k) = \begin{pmatrix} 0 & R \\ L & 0 \end{pmatrix}, \tag{S4}$$

where

$$R = \begin{pmatrix} f + \delta + Z & 2Z - i(Z + \sin(k + k_0)) \\ i(Z - \sin(k + k_0)) & f + \delta - Z \end{pmatrix}, \quad L = \begin{pmatrix} f - \delta + Z & -i(Z - \sin(k + k_0)) \\ 2Z + i(Z + \sin(k + k_0)) & f - \delta - Z \end{pmatrix}, \tag{S5}$$

and $f = \cos(k + k_0) + \cos k_0 - M$. For this $H_{y\text{-OBC}}(k)$, the topological edge bands exhibit two different types of dispersion relations around the EP: (1) a linear dispersion $E_e(\delta k) \sim \delta k$, as shown in Fig. 1(c), and (2) square-root dispersion $E_e(\delta k) \sim \sqrt{\delta k}$, as depicted in Fig. S1(a).

To explain why the dispersion can exhibit two qualitatively different behavior (i.e. becomes linear when we set Z = 1, $\delta = M - Z$ in Eq. (S3)), we expand the momentum k around the EP as: $k \to 0 + \delta k$. We shall prove that:

$$\det[H_{\text{y-OBC}}(\delta k)] \sim \begin{cases} \delta k^2, & \text{with } Z = 1, \delta = M - Z \\ \delta k, & \text{other parameters} \end{cases}$$
 (S6)

This is connected to the dispersion of the topological bands because the latter are the only ones that vanish (are gapless). To elaborate, we know that the determinant is equal to the product of all eigenenergies as:

$$\det[H_{y-OBC}(k)] = E_{e_1}(k)E_{e_2}(k) \prod_n E_n(k),$$
(S7)

where $E_{e_1}(k)$ and $E_{e_2}(k)$ are the two topological edge bands, and the $E_n(k)$ s represent bulk bands. As $\delta k \to 0$, $\det[H_{\text{y-OBC}}(\delta k)]$ approaches zero, as do $E_{e_1}(\delta k)$ and $E_{e_2}(\delta k)$ with $|E_{e_1}| = |E_{e_2}|$. However, the bulk bands $E_n(\delta k)$ approach finite values. Thus, the topological edge bands exhibit dispersions described by $E_{e_{1,2}} \sim \sqrt{\det(H_{\text{y-OBC}})}$. Below, we show that this $\sim \delta k$ when the parameters are set to Z = 1, $\delta = M - Z$. For other parameter combinations, $E_{e_{1,2}}$ will behave generically as $\sim \sqrt{\delta k}$.

To derive Eq. (S6), we first expand $H_{y\text{-OBC}}$ around k = 0. Since k appears only in the diagonal element h_0^y , we need to expand the R and L matrices [Eq. (S5)]. By substituting $\sin k_0 = Z$ into Eq. (S5), we obtain

$$\sin(k_0 + \delta k) \approx Z + \cos k_0 \delta k - \frac{Z}{2} \delta k^2, \qquad \cos(k_0 + \delta k) \approx \cos k_0 - Z \delta k - \frac{\cos k_0}{2} \delta k^2, \tag{S8}$$

and

$$R(\delta k) = \begin{pmatrix} R_{11} & R_{12} \\ R_{21} & R_{22} \end{pmatrix} = \begin{pmatrix} f_0 + \delta + Z & 2Z(1-i) \\ 0 & f_0 + \delta - Z \end{pmatrix} + \begin{pmatrix} -Z & -i\cos k_0 \\ -i\cos k_0 & -Z \end{pmatrix} \delta k + \begin{pmatrix} -\frac{1}{2}\cos k_0 & i\frac{Z}{2} \\ i\frac{Z}{2} & -\frac{1}{2}\cos k_0 \end{pmatrix} \delta k^2 + O(\delta k^3), \tag{S9}$$

where $f_0 = 2\cos k_0 - M$, and

$$L(\delta k) = \begin{pmatrix} L_{11} & L_{12} \\ L_{21} & L_{22} \end{pmatrix} = \begin{pmatrix} f_0 - \delta + Z & 0 \\ 2Z(1+i) & f_0 - \delta - Z \end{pmatrix} + \begin{pmatrix} -Z & i\cos k_0 \\ i\cos k_0 & -Z \end{pmatrix} \delta k + \begin{pmatrix} -\frac{1}{2}\cos k_0 & -i\frac{Z}{2} \\ -i\frac{Z}{2} & -\frac{1}{2}\cos k_0 \end{pmatrix} \delta k^2 + O(\delta k^3). \tag{S10}$$

Then, by using Schur's determinant identity, $\det \begin{pmatrix} A & B \\ C & D \end{pmatrix} = \det(D) \det(A - BD^{-1}C)$ [120], we can calculate $\det[H_{\text{y-OBC}}]$ as follows (for simplicity, we rewrite h_0^y as h_0):

$$\det\begin{pmatrix} h_{0} & h_{+} & \cdots & 0 \\ h_{-} & h_{0} & h_{+} & \vdots \\ 0 & h_{-} & \ddots & h_{+} \\ 0 & \cdots & h_{-} & h_{0} \end{pmatrix}_{L_{y}} = \det(h_{0}) \det\begin{pmatrix} h_{0} & h_{+} & \cdots & 0 \\ h_{-} & h_{0} & h_{+} & \vdots \\ 0 & h_{-} & \ddots & h_{+} \\ 0 & \cdots & h_{-} & h_{0}^{(1)} \end{pmatrix}_{L_{y}-1} = \det(h_{0}) \det(h_{0}^{(1)}) \det\begin{pmatrix} h_{0} & h_{+} & \cdots & 0 \\ h_{-} & h_{0} & h_{+} & \vdots \\ 0 & h_{-} & \ddots & h_{+} \\ 0 & \cdots & h_{-} & h_{0}^{(2)} \end{pmatrix}_{L_{y}-2} = \det(h_{0}) \det(h_{0}^{(1)}) \det(h_{0}^{(1)}) \cdot \cdots \cdot \det(h_{0}^{(L_{y}-1)}), \tag{S11}$$

in which

$$h_0^{(1)} = h_0 - h_+ h_0^{-1} h_- = \begin{pmatrix} 0 & R^{(1)} \\ L^{(1)} & 0 \end{pmatrix}, \qquad R^{(1)} = R - \begin{pmatrix} 0 & 0 \\ (R^{-1})_{21} & 0 \end{pmatrix}, \qquad L^{(1)} = L - \begin{pmatrix} 0 & (L^{-1})_{12} \\ 0 & 0 \end{pmatrix}$$

$$h_0^{(2)} = h_0 - h_+ [h_0^{(1)}]^{-1} h_- = \begin{pmatrix} 0 & R^{(2)} \\ L^{(2)} & 0 \end{pmatrix}, \qquad R^{(2)} = R - \begin{pmatrix} 0 & 0 \\ [(R^{(1)})^{-1}]_{21} & 0 \end{pmatrix}, \qquad L^{(2)} = L - \begin{pmatrix} 0 & [(L^{(1)})^{-1}]_{12} \\ 0 & 0 \end{pmatrix}, \tag{S12}$$

and so forth $h_0^{(n)} = h_0 - h_+ [h_0^{(n-1)}]^{-1} h_-$. Now, to calculate Eq. (S11), we need to determine how $\det(h_0^{(n)})$ varies with δk .

• For the case considered in the main text with $\lambda = Z = 1, \delta = M - Z, k_0 = \pi/2$, we have

$$R(\delta k) = \begin{pmatrix} -\delta k & 2(1-i) + \frac{i}{2}\delta k^2 \\ \frac{i}{2}\delta k^2 & -2 - \delta k \end{pmatrix} + O(\delta k^3), \quad L(\delta k) = \begin{pmatrix} 2(1-M) - \delta k & -\frac{i}{2}\delta k^2 \\ 2(1+i) - \frac{i}{2}\delta k^2 & -2M \end{pmatrix} + O(\delta k^3), \tag{S13}$$

and $det(R) \approx 2\delta k$, $det(L) \approx -4M(1-M) + 2M\delta k$, which gives us:

$$\det(h_0) = \det(R)\det(L) \approx -8M(1-M)\delta k. \tag{S14}$$

Importantly, the fact that det R is proportional to $2\delta k$ and vanishes as $\delta k \to 0$ will turn out to be crucial. According to Eq. (S12), for the first iteration, det $(h_0^{(1)})$, can be calculated using $R^{(1)}$ and $L^{(1)}$

$$R^{(1)} = \begin{pmatrix} R_{11} & R_{12} \\ R_{21} - (R^{-1})_{21} & R_{22} \end{pmatrix} = \begin{pmatrix} R_{11} & R_{12} \\ (1 + \frac{1}{\det(R)})R_{21} & R_{22} \end{pmatrix} \approx \begin{pmatrix} -\delta k & 2(1-i) + \frac{i}{2}\delta k^{2} \\ \frac{i}{4}\delta k + \frac{i}{2}\delta k^{2} & -2 - \delta k \end{pmatrix} + O(\delta k^{3}),$$

$$L^{(1)} = \begin{pmatrix} L_{11} & L_{12} - (L^{-1})_{12} \\ L_{21} & L_{22} \end{pmatrix} = \begin{pmatrix} L_{11} & \left(1 - \frac{1}{4M(1-M)}\right)L_{12} \\ L_{21} & L_{22} \end{pmatrix} \approx \begin{pmatrix} 2(1-M) - \delta k & -\frac{i}{2}\left(1 - \frac{1}{4M(1-M)}\right)\delta k^{2} \\ 2(1+i) - \frac{i}{2}\delta k^{2} & -2M \end{pmatrix} + O(\delta k^{3}), \quad (S15)$$

with $\det(R^{(1)}) \approx (2 + \frac{1+i}{2})\delta k$, $\det(L^{(1)}) \approx -4M(1-M)$ and

$$\det(h_0^{(1)}) = \det(R^{(1)}) \det(L^{(1)}) \approx -4M(1 - M) \left(2 + \frac{1 + i}{2}\right) \delta k.$$
 (S16)

For the second and subsequent iterations $(n \ge 2)$, the elements $R_{11/12/22}^{(n)}$ and $L_{11/21/22}^{(n)}$ remain unchanged. And for element $[R^{(n)}]_{21}$, we have

$$[R^{(2)}]_{21} = R_{21} - [(R^{(1)})^{-1}]_{21} = R_{21} + \frac{R_{21}^{(1)}}{\det(R^{(1)})} \approx \frac{i}{10 + 2i} = \text{Const}, \quad \det(R^{(2)}) \approx -\frac{1 + i}{5 + i} = \text{Const},$$

$$[R^{(n)}]_{21} = R_{21} - [(R^{(n-1)})^{-1}]_{21} = R_{21} + \frac{R_{21}^{(n-1)}}{\det(R^{(n-1)})} = \frac{i}{2}\delta k^2 + \frac{\text{Const}}{\text{Const}} \approx \text{Const},$$

$$\det(R^{(n)})|_{n \geq 2} \approx 2(1 - i) * [R^{(n)}]_{21} = \text{Const},$$
(S17)

and for $[L^{(n)}]_{12}$,

$$[L^{(2)}]_{12} = L_{12} - [(L^{(1)})^{-1}]_{12} = -\frac{i\delta k^2}{2} + \frac{L_{12}^{(1)}}{\det(L^{(1)})} \approx \frac{i\delta k^2}{2} \left(\frac{1 - \frac{1}{4M(1-M)}}{4M(1-M)} - 1\right), \det(L^{(2)}) \approx -4M(1-M) = \text{Const},$$

$$[L^{(n)}]_{12} = L_{12} + \frac{L_{12}^{(n-1)}}{\det(L^{(n-1)})} \sim \delta k^2, \qquad \det(L^{(n)})|_{n\geq 2} \approx -2(1-M) * 2M = -4M(1-M) = \text{Const}.$$
(S18)

Therefore, for $n \ge 2$, the determinant $\det(h_0^{(n)})$ remains constant, leading to the quadratic dispersion:

$$\det(H_{y-OBC}) = \det(h_0) \det(h_0^{(1)}) \cdots \det(h_0^{(L_y-1)}) \sim \delta k^2.$$
 (S19)

• For most other generic parameter combinations, such as the case shown in Fig. S1(a), the constant term in det(R) does not vanish i.e., $det(R) \rightarrow Const$ as $\delta k \rightarrow 0$. Below we show how that leads to a qualitatively different dispersion. We have

$$\det(R) \approx (f_0 + \delta)^2 - Z^2 - 2Z(f_0 + \delta - (1+i)\cos k_0)\delta k = C_0^R + C_1^R \delta k,$$

$$\det(L) \approx (f_0 - \delta)^2 - Z^2 - 2Z(f_0 - \delta + (1-i)\cos k_0)\delta k = C_0^L + C_1^L \delta k,$$

$$\det(h_0) = \det(R)\det(L) \approx C_0^R C_0^L + (C_0^R C_1^L + C_0^L C_1^R)\delta k.$$
(S20)

where $C_0^{R(L)}$ and $C_1^{R(L)}$ are constants. For the first iteration, we have

$$R^{(1)} = \begin{pmatrix} R_{11} & R_{12} \\ R_{21} - (R^{-1})_{21} & R_{22} \end{pmatrix} \approx \begin{pmatrix} R_{11} & R_{12} \\ (1 + \frac{1}{C_0^R})R_{21} & R_{22} \end{pmatrix}, \quad \det(R^{(1)}) \approx C_0^{(1)R} + C_1^{(1)R}\delta k,$$

$$L^{(1)} = \begin{pmatrix} L_{11} & L_{12} - (L^{-1})_{12} \\ L_{21} & L_{22} \end{pmatrix} \approx \begin{pmatrix} L_{11} & (1 + \frac{1}{C_0^L})L_{12} \\ L_{21} & L_{22} \end{pmatrix}, \quad \det(L^{(1)}) \approx C_0^{(1)L} + C_1^{(1)L}\delta k,$$

$$\det(h_0^{(1)}) = \det(R^{(1)})\det(L^{(1)}) \approx C_0^{(1)R}C_0^{(1)L} + (C_0^{(1)R}C_1^{(1)L} + C_0^{(1)L}C_1^{(1)R})\delta k. \tag{S21}$$

By analogy, for $n \ge 2$, we have

$$[R^{(n)}]_{21} = R_{21} - [(R^{(n-1)})^{-1}]_{21} = R_{21} + \frac{[R^{(n-1)}]_{21}}{\det(R^{(n-1)})} \sim R_{21}, \quad \text{and similarly,} \quad [L^{(n)}]_{12} \sim L_{12}, \tag{S22}$$

which ensures that the expansion of $\det(h_0^{(n)}) = \det(R^{(n)}) \det(L^{(n)}) \sim \det(h_0)$ always remains in the form of $C_0^{(n)} + C_1^{(n)} \delta k$. Therefore, in this case, we can obtain the linear dispersion of $\det(H_{\text{V-OBC}})$ as:

$$\det(H_{y-OBC}) = \det(h_0) \det(h_0^{(1)}) \cdots \det(h_0^{(L_y-1)})$$

$$\approx (C_0 + C_1 \delta k) * (C_0^{(1)} + C_1^{(1)} \delta k) \cdots (C_0^{(L_y-1)} + C_1^{(L_y-1)} \delta k) \sim \delta k,$$
(S23)

where the constant term $C_0C_0^{(1)}\cdots C_0^{(L_y-1)}$ goes to zero due to the existence of zero energy modes as shown in Fig. S1(a).

The above approach hinges on the observation that the two types of dispersion are distinguished by whether $\det(R) = 0$. It works for models where most matrix elements in h_{+}^{y} and h_{-}^{y} are 0, which effectively simplifies the calculation of $h_{0}^{(n)} = h_{0} - h_{+} [h_{0}^{(n-1)}]^{-1} h_{-}$ in Eq. S11. In more general models with hoppings beyond nearest neighbors, Eq. S11 would need to be extended to handle multiple matrix diagonals, and this iterative approach could become far more complicated.

II. DETAILED ANALYSIS OF THE TOPOLOGICAL FLAT BAND MODEL

In this section, we analyze the two-band model introduced in Eq. (9) of the main text

$$H(k, k_{v}) = t \cos k_{v} \sigma_{x} + (a_{0} - t \sin k_{v})\sigma_{+} + ((b_{0} - \cos k)^{B} + t \sin k_{v})\sigma_{-},$$
 (S24)

which possesses topological flat bands that experience the NHSE.

A. Exponential scaling of the topological gap with L_{ν}

Here, we show that the topological gap Δ of our flat band model exhibits exponential decay with respect to the system size L_y within the topologically non-trivial regime. Considering OBCs in the y-direction, as similarly analyzed in the previous section, the Hamiltonian can be expressed as follows:

$$H_{y-OBC}(k) = \begin{pmatrix} h_0^y & h_+^y & \cdots & 0 & 0 \\ h_-^y & h_0^y & h_+^y & \cdots & 0 \\ 0 & h_-^y & h_0^y & \cdots & 0 \\ \vdots & \vdots & \ddots & \ddots & \vdots \\ 0 & 0 & \cdots & h_-^y & h_0^y \end{pmatrix}_{L_y \times L_y} \text{ with } h_0^y = \begin{pmatrix} 0 & a_0 \\ (b_0 - \cos k)^B & 0 \end{pmatrix}, h_+^y = \begin{pmatrix} 0 & 0 \\ t & 0 \end{pmatrix}, h_-^y = \begin{pmatrix} 0 & t \\ 0 & 0 \end{pmatrix}.$$
 (S25)

Specifically, they satisfy the equation $h_{+}^{y}(h_{0}^{y})^{-1}h_{-}^{y}=0$. Therefore, for this model, we have

$$\det(H_{y\text{-OBC}}(k)) = \det(h_0^y) \det\begin{pmatrix} h_0^y & h_+^y & \cdots & 0 \\ h_-^y & h_0^y & \cdots & 0 \\ \vdots & \ddots & \ddots & \vdots \\ 0 & \cdots & h_-^y & h_0^y - h_+^y (h_0^y)^{-1} h_-^y \end{pmatrix} = \det(h_0^y) \det\begin{pmatrix} h_0^y & h_+^y & \cdots & 0 \\ h_-^y & h_0^y & \cdots & 0 \\ \vdots & \ddots & \ddots & \vdots \\ 0 & \cdots & h_-^y & h_0^y \end{pmatrix}_{(L_y - 1) \times (L_y - 1)}$$

$$= \left(\det(h_0^y)\right)^{L_y} = \left(a_0(b_0 - \cos k)^B\right)^{L_y}. \tag{S26}$$

To account for the NHSE experienced by system, we can perform a basis transform to the surrogate Hamiltonian [121]. Since $H_{y\text{-OBC}}$ can be viewed as a non-Hermitian SSH model with k-dependent, asymmetric intra-cell hopping amplitudes a_0 and $b_0 - \cos k$, Therefore, akin to the non-Hermitian SSH model [94], we can apply a similarity transformation to $H_{y\text{-OBC}}$,

$$H'(k) = Q^{-1}H_{y-OBC}(k)Q, \quad Q = \operatorname{diag}\{1, r, r, r^2, \cdots r^{L_y-1}, r^{L_y-1}, r^{L_y}\}, \quad r = \sqrt{\left|\frac{(b_0 - \cos k)^B}{a_0}\right|}, \tag{S27}$$

and obtain a Hermitian matrix H'(k):

$$H'(k) = \begin{pmatrix} 0 & te^{-ik_y} + t' \\ te^{ik_y} + t' & 0 \end{pmatrix}, \text{ where } t' = \sqrt{a_0(b_0 - \cos k)^B}.$$
 (S28)

Since a similarity matrix transform does not change the eigenspectrum, H'(k) possesses the same eigenvalues as $H_{y\text{-OBC}}$, with its bulk eigenvalues given by $E_n = \pm \sqrt{(te^{ik_y} + t')(te^{-ik_y} + t')}$. By substituting these values of E_n into $\det[H_{y\text{-OBC}}(k)] = E_{e_1}(k)E_{e_2}(k)\prod_n E_n(k)$, we obtain

$$\prod_{n} E_{n}(k) = -\prod_{k_{y}} (te^{ik_{y}} + t')(te^{-ik_{y}} + t') \sim t^{2L_{y}} + c_{1}t^{2L_{y}-1}t' + c_{2}t^{2L_{y}-2}t'^{2} + \dots + c_{L_{y}}t'^{2L_{y}},$$
 (S29)

where in the RHS, the terms containing $e^{\pm ik_y}$ are incorporated into the coefficients $c_1, c_2, ..., c_{L_y}$. As mentioned in the main text, the topological non-trivial condition is $|a_0(b_0 - \cos k)^B| \le t^2$, i.e. $|t'| \le |t|$. Consequently, the leading term in the RHS of the above equation is t^{2L_y} . Then using Eq. (S29), we have

$$\det[H_{y\text{-OBC}}(k)] = E_{e_1}(k)E_{e_2}(k) * t^{2L_y} (1 + O(t'/t)) = \left(a_0(b_0 - \cos k)^B\right)^{L_y}$$

$$E_{e_1}(k)E_{e_2}(k) \approx \frac{\left(a_0(b_0 - \cos k)^B\right)^{L_y}}{t^{2L_y}}.$$
(S30)

And because $E_{e_1} = -E_{e_2}$, we ultimately obtain the scaling of topological gap Δ with L_y as follows:

$$\Delta = 2|E_{e_1}| \sim \left(\frac{a_0(b_0 - \cos k)^B}{t^2}\right)^{L_y/2}.$$
 (S31)

B. Scaling of entanglement entropy S_A with system sizes L and L_y in the case of gapless flat bands

In this subsection, we derive the scaling relations of S_A as a function of L_y and L_y , specifically Eq. (14) in the main text:

$$S_A \sim -\frac{1}{2}(BL_y)^2 \log L \tag{S32}$$

for the gapless case of $b_0 = 1$. This is a highly unusual scaling behavior because S_A scales faster than L_y , the number of states (volume) from the y-dimension. Below we shall elucidate the origin of this super volume-law entanglement scaling behavior. While it may naively appear that this extra factor of BL_y scaling (quadratic vs. linear i.e. volume-law) originates from the high-order topological flat band dispersion $E(k) \sim k^{BL_y}$, below we shall show that the full story is more complicated, crucially involving the NHSE.

To establish the scaling relation of S_A , we first need to prove that:

$$Tr(\bar{P}^2) = \sum_{i} p_i^2 \sim c_1 L^{BL_y - 1} + c_2 L^{BL_y - 1 - 2} + \dots + \dots,$$
 (S33)

where p_i represents the eigenvalues of \bar{P} , and $c_1, c_2, ...$ are coefficients that are independent of L. In other words, that the eigenvalues p_i of \bar{P} scales like various powers of L, up to L^{BL_y-1} .

Below, we present a comprehensive derivation of Eq. (S33). Under OBCs in the y direction, k is still a good eigenstate label and the projector operator in k space is defined as $P(k) = \sum_{n \in occ} |\psi_n(k)^R\rangle \langle \psi_n(k)^L|$. Due to the NHSE which pushes all right eigenstates in the y-direction towards the same edge, they become highly edge-localized and hence almost orthogonal. This large overlap ensures that the corresponding left edge eigenstates exhibit large amplitudes and contribute most significantly to P(k). Therefore, P(k) is dominated by the edge state contributions:

$$P(k) = \sum_{n \in occ} |\psi_n(k)^R\rangle \langle \psi_n(k)^L|$$

$$\approx |\psi_{edge}(k)^R\rangle \langle \psi_{edge}(k)^L| = P_{edge}(k). \tag{S34}$$

In the following discussion, for the sake of brevity, we will omit the k in $|\psi_{edge}(k)^R\rangle$, $\langle\psi_{edge}(k)^L|$, rewriting them as $|\psi_{edge}^R\rangle$, $\langle\psi_{edge}^L|$. To proceed, we note that $P_{edge}(k)$ is furthermore dominated by just *one* matrix element due to the exponential skin-localization of the edge states. To show this explicitly, we use the similarity transform [Eq. (S28)] to write the spatial profiles of the topological SSH edge states in the y direction as

$$|\psi'_{edge}(y)\rangle = \begin{pmatrix} \psi'^{A}(y) \\ \psi'^{B}(y) \end{pmatrix} \sim \begin{pmatrix} \epsilon^{y-1} \\ \epsilon^{L_{y}-y} \end{pmatrix}, \quad \text{where } \epsilon = \left| \frac{t'}{t} \right| = \sqrt{\left| \frac{a_0}{t} (b_0 - \cos k)^B \right|}.$$
 (S35)

Consequently, the right and left edge states of the original H_{y-OBC} is given by

$$|\psi_{edge}^{R}\rangle = Q|\psi_{edge}'\rangle \sim \begin{pmatrix} \begin{pmatrix} 1\\ re^{L_{y}-1} \end{pmatrix}\\ r\begin{pmatrix} \epsilon\\ re^{L_{y}-2} \end{pmatrix}\\ \vdots\\ r^{L_{y}-2}\begin{pmatrix} \epsilon^{L_{y}-2} \\ r\epsilon\\ r^{L_{y}-1}\begin{pmatrix} \epsilon^{L_{y}-1} \end{pmatrix} \end{pmatrix}, \quad \text{and} \quad \langle \psi_{edge}^{L}| = Q^{-1}\langle \psi_{edge}' | \sim \begin{pmatrix} \begin{pmatrix} 1\\ \epsilon^{L_{y}-1}/r \end{pmatrix}\\ \frac{1}{r}\begin{pmatrix} \epsilon\\ \epsilon^{L_{y}-2}/r \end{pmatrix}\\ \vdots\\ \frac{1}{r^{L_{y}-2}}\begin{pmatrix} \epsilon^{L_{y}-2}\\ \epsilon/r \end{pmatrix}\\ \frac{1}{r^{L_{y}-1}}\begin{pmatrix} \epsilon^{L_{y}-1}\\ 1/r \end{pmatrix} \end{pmatrix}. \tag{S36}$$

This yields the following form for the projector matrix

$$P(k) \approx P_{edge}(k) = |\psi_{edge}^{R}\rangle \langle \psi_{edge}^{L}| \sim \begin{pmatrix} 1 & \epsilon^{L_{y}-1}/r \\ r\epsilon^{L_{y}-1} & \epsilon^{2L_{y}-2} \end{pmatrix} & \frac{1}{r} \begin{pmatrix} \epsilon & \epsilon^{L_{y}-2}/r \\ r\epsilon^{L_{y}} & \epsilon^{2L_{y}-3} \end{pmatrix} & \cdots & \frac{1}{r^{L_{y}-1}} \begin{pmatrix} \epsilon^{L_{y}-1} & 1/r \\ r\epsilon^{2L_{y}-2} & \epsilon^{L_{y}-1} \end{pmatrix} \\ r \begin{pmatrix} \epsilon & \epsilon^{L_{y}}/r \\ r\epsilon^{L_{y}-2} & \epsilon^{L_{y}-2} \end{pmatrix} & \begin{pmatrix} \epsilon^{2} & \epsilon^{L_{y}-1}/r \\ r\epsilon^{L_{y}-1} & \epsilon^{2L_{y}-4} \end{pmatrix} & \cdots & \frac{1}{r^{L_{y}-2}} \begin{pmatrix} \epsilon^{L_{y}} & \epsilon/r \\ r\epsilon^{2L_{y}-3} & \epsilon^{L_{y}-2} \end{pmatrix} \\ \vdots & \vdots & \vdots & \vdots \\ r^{L_{y}-1} \begin{pmatrix} \epsilon^{L_{y}-1} & \epsilon^{2L_{y}-2}/r \\ r & \epsilon^{L_{y}-1} \end{pmatrix} & r^{L_{y}-2} \begin{pmatrix} \epsilon^{L_{y}} & \epsilon^{2L_{y}-3}/r \\ r\epsilon & \epsilon^{L_{y}-2} \end{pmatrix} & \cdots & \begin{pmatrix} \epsilon^{2L_{y}-2} & \epsilon^{L_{y}-1}/r \\ r\epsilon^{L_{y}-1} & 1 \end{pmatrix} \end{pmatrix}_{2L_{y}\times 2L_{y}}$$
(S37)

which is dominated by the upper right matrix element in blue, since $r = \sqrt{\frac{(b_0 - \cos k)^B}{a_0}} < 1$ for the parameters used.

The truncated projector \bar{P} can be obtained by Fourier transforming each matrix element on the right-hand side (RHS) of Eq. (S37) i.e.

$$\bar{P} = \begin{pmatrix} \bar{P}_{1,1} & \bar{P}_{1,2} & \cdots & \bar{P}_{1,2L_y} \\ \bar{P}_{2,1} & \bar{P}_{2,2} & \cdots & \bar{P}_{2,2L_y} \\ \vdots & \vdots & \ddots & \vdots \\ \bar{P}_{2L_y,1} & \bar{P}_{2L_y,2} & \cdots & \bar{P}_{2L_y,2L_y} \end{pmatrix}, \text{ where } \bar{P}_{m,n} \text{ is an } l \times l \text{ matrix whose elements are } \langle x_1 | \bar{P}_{m,n} | x_2 \rangle = \frac{1}{L} \sum_k e^{ik(x_1 - x_2)} P_{m,n}(k),$$
(S38)

with l denoting the size of subregion A and $x_1, x_2 \in A$. The dominant submatrix $\bar{P}_{1,2L_y}(k)$ is, after Fourier transformation into real space and substituting $r = \sqrt{\left|\frac{(b_0 - \cos k)^B}{a_0}\right|}$, given by

$$\langle x_{1} | \bar{P}_{1,2L_{y}} | x_{2} \rangle = \frac{1}{L} \sum_{k} e^{ik(x_{1}-x_{2})} P_{1,2L_{y}}(k)$$

$$\sim \frac{1}{L} a_{0}^{L_{y}/2} \frac{2 \cos(k_{1}(x_{1}-x_{2}))}{(b_{0}-\cos k_{1})^{BL_{y}/2}}$$

$$\sim a_{0}^{L_{y}/2} \left(\frac{L}{\pi}\right)^{BL_{y}-1} \times \left(1 - \frac{1}{2}(\frac{\pi x}{L})^{2} + \frac{1}{4!}(\frac{\pi x}{L})^{4} - \frac{1}{6!}(\frac{\pi x}{L})^{6} + \cdots\right)$$

$$= c_{1} L^{BL_{y}-1} + c_{2} L^{BL_{y}-1-2} + \cdots, \tag{S39}$$

with $b_0 = 1$ and the leading $k = \pm k_1 = \pm \pi/L$ contributions substituted to obtain the 3rd line. The other matrix elements scale more slowly with L. Since $\langle x_1 | \bar{P}_{2L_y,1} | x_2 \rangle \sim O(1)$, we have established Eq. S33:

$$\operatorname{Tr}(\bar{P}^2) \approx 2\operatorname{Tr}(\bar{P}_{1,2L_y}\bar{P}_{2L_y,1}) \sim c_1 L^{BL_y-1} + c_2 L^{BL_y-1-2} + \cdots$$
 (S40)

where, as a first-order approximation, we have retained only the term containing the largest block $P_{1,2L_y}$ and disregarded the contributions from other elements. This implies that the eigenvalues p_i generically scale like $p_i \sim cL^{\alpha}$ with c an unimportant constant. For odd BL_y , $\alpha = 1, 2..., (BL_y - 1)/2$ and for even BL_y , $\alpha = 1/2, 3/2, ..., (BL_y - 1)/2$.

For each $p_i = cL^{\alpha}$ (c is a constant), its contribution to entanglement entropy S_A is

$$S_{A}(p_{i}) = -p_{i} \log p_{i} - (1 - p_{i}) \log(1 - p_{i}) = -cL^{\alpha} \log(cL^{\alpha}) - (1 - cL^{\alpha}) \log(1 - cL^{\alpha})$$

$$= -cL^{\alpha} \log(cL^{\alpha}) + cL^{\alpha} \log(1 - cL^{\alpha}) - \log(1 - cL^{\alpha})$$

$$\approx -cL^{\alpha} \log(cL^{\alpha}) + cL^{\alpha} \log(-cL^{\alpha}) - \log(1 - cL^{\alpha})$$

$$= (cL^{\alpha} + 1) \log(-1) - \log(cL^{\alpha}) \approx -\alpha \log L + cL^{\alpha}\pi i - \log c.$$
(S41)

The other eigenvalue with $p'_i = 1 - p_i$ (see Sect. III.B) contributes the same real part to S_A , but opposite imaginary part that cancels off, as numerically observed as twofold degenerate states. Therefore, the total entanglement entropy is dominated by the log L contribution in blue above which should be multiplied by 4, i.e.

$$S_A = \sum_{p_i} -p_i \log p_i - (1 - p_i) \log(1 - p_i) \sim -4 \times \left[\frac{BL_y - 1}{2} + \left(\frac{BL_y - 1}{2} - 1 \right) + \left(\frac{BL_y - 1}{2} - 2 \right) + \cdots \right] \log L. \tag{S42}$$

Calling $J = \frac{BL_y - 1}{2}$ $(B, L_y \in \mathbb{Z})$ and $J' = \lceil J \rceil = \begin{cases} J, & BL_y \text{ is odd} \\ J + 1/2, & BL_y \text{ is even} \end{cases}$, we finally obtain the scaling relation of S_A with L, L_y as

$$S_{A} \sim -4 \log L \Big(J + (J - 1) + (J - 2) + \dots + (J - J' + 1) \Big)$$

$$= -2J'(2J - J' + 1) \log L$$

$$= -\frac{1}{2} \Big((BL_{y})^{2} - (BL_{y} \text{mod} 2) \Big) \log L$$

$$= -\left[\frac{B^{2}L_{y}^{2} - 1}{2} \right] \log L \sim -\frac{1}{2} (BL_{y})^{2} \log L, \tag{S43}$$

which is our key super volume-law negative entanglement scaling result.

Below, we further present the numerical verification of Eq. (S42). In Fig. S4(a), we take $L_y = 3$, B = 1, since $\frac{BL_y-1}{2} = 1$, only the first order $p_i \sim L^1$ exists. The numerical fitting shown in Fig. S4(d) yields:

$$S_A \sim -4.4072 \log L \quad \approx -4 \times \frac{BL_y - 1}{2} \log L = -4 \log L,$$
 (S44)

which demonstrates good agreement with Eq. (S42). In Fig. S4(b), where $L_y = 5$, B = 1, $\frac{BL_y-1}{2} = 2$, both the first and second orders of L in $p_i \sim L^1$, $p_i \sim L^2$ are present. We numerically obtain the scaling of entanglement entropy as depicted in Fig. S4(e):

$$S_A \sim -11.7648 \log L \approx -4 \times \left(\frac{BL_y - 1}{2} + \frac{BL_y - 1}{2} - 1\right) \log L = -12 \log L.$$
 (S45)

For the case of $L_y = 3$, B = 2 shown in Fig. S4(c), the first, second and third orders of L all contribute to the EE:

$$S_A \sim -17.1980 \log L \approx -4 \times \left(\frac{BL_y - 1}{2} + \frac{BL_y - 1}{2} - 1 + \frac{BL_y - 1}{2} - 2\right) \log L = -18 \log L.$$
 (S46)

While plots with even larger L_y and B would be more prone to numerical errors due to the larger L needed, excellent agreement is already observed for this cases which corresponds to the most realistic models.

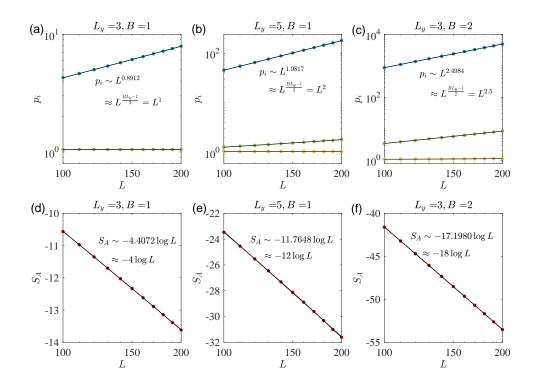


FIG. S4. Excellent agreement of our super volume-law negative entanglement scaling result with numerics for various B and L_y , both for the \bar{P} eigenvalues p_i [Eq. S33] (a-c) and the corresponding entanglement scaling $S_A \sim -\left[(B^2L_y^2-1)/2\right]\log L$ [Eq. S43]. Parameters: $t=0.5, a_0=2, b_0=1$.

C. Scaling of entanglement entropy S_A for gapped flat bands

In the case of gapped bands where $b_0 > 1$ (e.g., $b_0 = 1.2$), there exists a small gap Δ (see Eq. (S31)) in the topological flat edge bands. Due to this gap, the entanglement entropy S_A decreases with increasing system size L and eventually stabilizes at a minimum constant value, S_{min} . In this section, we will demonstrate that:

- 1) For $L \ll L_y$, S_A exhibits an approximate negative L_y -linear scaling with $\log L$, expressed as $S_A \sim -(\alpha L_y + \beta) \log L$, where α and β are fitting coefficients with $\alpha > 0$;
- 2) While for $L \gg L_y$, S_A saturates to the lower bound, S_{min} , which scales linearly with L_y as: $S_{min} \sim -L_y \log \left(\frac{a_0}{(b_0-1)^8}\right)$.

In the preceding subsection II.B, we demonstrated that near k = 0, the dominant element of P(k) is located in the upper right corner, where $P_{1,2L_y}(k) \sim 1/r^{L_y}$ with $r = \sqrt{\left|\frac{(b_0 - \cos k)^B}{a_0}\right|} < 1$. For $b_0 > 1$, this can still be the case with appropriate choice of a_0 . We have

$$\langle x_1 | \bar{P}_{1,2L_y} | x_2 \rangle = \frac{1}{L} \sum_{k} e^{ik(x_1 - x_2)} P_{1,2L_y}(k) \qquad \sim \frac{1}{L} \sum_{k} e^{ik(x_1 - x_2)} a_0^{L_y/2} \frac{1}{(b_0 - \cos k)^{BL_y/2}}, \tag{S47}$$

where k takes the values π/L , $3\pi/L$, $5\pi/L$, For $k_1 = \pi/L$, which contributes most significantly to $\langle x_1 | \bar{P}_{1,2L_y} | x_2 \rangle$, we have

$$(b_0 - \cos k_1)^{BL_y/2} = (b_0 - 1 + 1 - \cos k_1)^{BL_y/2} = (b_0 - 1)^{BL_y/2} (1 + x)^{BL_y/2},$$
 (S48)

where $x = \frac{1-\cos k_1}{b_0-1} \approx \frac{\pi^2}{2(b_0-1)L^2}$. When $L \ll L_y$, (for simplicity, we select L_y to be an even number to ensure $BL_y/2$ is an integer), the following approximation

$$(1+x)^{BL_y} = \sum_{m} C_{BL_y/2}^m x^m \approx C_{BL_y/2}^M x^M$$
 (S49)

where m = M represents the maximum term in the summation. As verified in Fig. S5(a), M exhibits a linear relation with L_{γ} , expressed as $M \approx \frac{1}{2}(\gamma L_y + \zeta)$ (where γ, ζ are coefficients independent of L_y). Consequently, we find

$$(1+x)^{BL_{y}} \approx C_{BL_{y}/2}^{M} \times C_{BL_{y}/2}^{(\gamma L_{y}+\zeta)/2} \left(\frac{\pi^{2}}{2(b_{0}-1)L^{2}}\right)^{(\gamma L_{y}+\zeta)/2} \sim L^{-(\gamma L_{y}+\zeta)}.$$
 (S50)

By substituting into Eq. (S48) and (S47) and considering only the contribution from $k_1 = \pi/L$, we have

$$\langle x_1 | \bar{P}_{1,2L_y} | x_2 \rangle \sim \frac{1}{L} e^{ik_0(x_1 - x_2)} \frac{a_0^{L_y/2}}{(b_0 - 1)^{BL_y/2} (1 + x)^{BL_y/2}} \sim L^{\gamma L_y + \zeta - 1}.$$
 (S51)

As we have demonstrated in the previous subsection B, since the elements of $\bar{P}_{1,2L_y}$ are proportional to $L^{\gamma L_y + \zeta - 1}$, we can deduce:

$$\operatorname{Tr}(\bar{P}^{2}) \approx 2\operatorname{Tr}(\bar{P}_{1,2L_{y}}\bar{P}_{2L_{y},1}) \sim L^{\gamma L_{y}+\zeta-1} \Longrightarrow p_{i}^{1st} \sim L^{\frac{\gamma L_{y}+\zeta-1}{2}}$$

$$S_{A} \sim -4 \times \left(\frac{\gamma L_{y}+\zeta-1}{2}\right) \log L \sim -(\alpha L_{y}+\beta) \log L, \tag{S52}$$

where we have redefined 2γ as α and $2(\zeta - 1)$ as β . In the $L \ll L_{\gamma}$ regime, higher orders of p_i are negligible, and we only need to consider the first order. Therefore, we conclude: for $L \ll L_{\gamma}$, $S_A \sim -\log L$ (Fig. S5(b)), with the gradient depending linearly on L_y (see Fig. S5(c)). Even though our derivation had assumed $L \ll L_y$, from the numerics in Fig. 2(e) of the main text, we see that this trend still mostly holds as long as $L < L_v$.

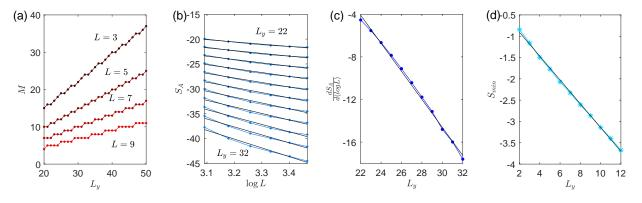


FIG. S5. Negative entanglement scaling for the gapped EP case $(b_0 > 1)$. (a) As numerically plotted for L = 9, $b_0 = 1.2$, the approximate linear scaling of the scaling exponent M of the dominant \bar{P} eigenvalue with L_v , as described by Eq. (S49). (b) The negatively linear relationship of the entanglement entropy S_A with $\log L$ for different L_v ranging from 22 to 32, with $L \in [22, 32]$ and parameters $t = 0.8, a_0 = 1, b_0 = 1.2, B = 1$. As predicted in Eq. (S52), the gradient indeed increases with L_v . (c) Using the same parameters as in (b), approximate linear dependence of the gradient of S_A on L_v . (d) For large L = 60 and parameters t = 0.8, B = 1, $L_v = 1.2$, L_v in Eq. (S55).

When $L \gg L_v$, Eq. (S48) can be approximated as:

$$(b_0 - \cos k_0)^{BL_y/2} = \left(b_0 - 1 + \frac{1}{2!} \left(\frac{\pi}{L}\right)^2 - \frac{1}{4!} \left(\frac{\pi}{L}\right)^4 + \cdots\right)^{BL_y/2}$$

$$\approx (b_0 - 1)^{BL_y/2}.$$
(S53)

Thus, Eq. (S47), which represents the elements of the largest matrix block $\bar{P}_{1,2L_v}$, can be expressed as

$$\langle x_1 | \bar{P}_{1,2L_y} | x_2 \rangle \sim \left(\frac{a_0}{(b_0 - 1)^B} \right)^{L_y/2} .$$
 (S54)

Following a similar derivation as Eq. (S52), we now have

$$\operatorname{Tr}(\bar{P}^{2}) \sim \left(\frac{a_{0}}{(b_{0}-1)^{B}}\right)^{L_{y}/2}, \quad p_{i}^{1st} \sim \left(\frac{a_{0}}{(b_{0}-1)^{B}}\right)^{L_{y}/4}$$

$$S_{min} \sim -4 \times \frac{L_{y}}{4} \log \left(\frac{a_{0}}{(b_{0}-1)^{B}}\right) = -L_{y} \log \left(\frac{a_{0}}{(b_{0}-1)^{B}}\right). \tag{S55}$$

This linear dependence on L_y is verified in Fig. S5(d). Empirically, we also see from Fig. 2(e) of the main text that this saturation generally sets in as long as L exceeds L_y .

III. FURTHER PROPERTIES OF THE NEGATIVE ENTANGLEMENT

A. Negativity of the Rényi entropy

Below, we show that when the entanglement entropy is negative, so is the Rényi entropy. For $|p_i| \gg 1$, we observe that $p_i^n + (1 - p_i)^n \propto |p_i|^n \gg 1$ for even-order n, and $p_i^n + (1 - p_i)^n \propto |p_i|^{n-1} \gg 1$ when n is odd. Substituting this p_i into Eq. (3) makes it is evident that the nth-order Rényi entropy will be negative. Similarly, for the von Neumann entropy as detailed in Eq. (4), the contribution of p_i to the real part of S_A , when $p_i \gg 1$, is given by

$$Re[S_A(p_i)] = -p_i \log(p_i) + (p_i - 1) \log(p_i - 1) < 0,$$
(S56)

and for $p_i \ll 0$, the contribution is

$$Re[S_A(p_i)] = |p_i| \log(|p_i|) - (|p_i| + 1) \log(|p_i| + 1) < 0.$$
(S57)

Thus, eigenvalues with $|p_i| \gg 1$ significantly contribute to a negative value for both the von Neumann and the nth-order $(n \ge 2)$ Rényi entropies.

B. PT-symmetry-protected real entanglement entropy S_A in the flat band model

In this section, we will demonstrate that the entanglement entropy S_A is rigorously real for PT-symmetry-protected models, including our topological flat band model. This can be attributed to the fact that the eigenvalues, p_i , of \bar{P} consistently appear as complex conjugate pairs.

First, in the $H_{\text{y-OBC}}(k)$ model of Eq. (S25), the parameters a_0, b_0, t are always real numbers, with $b_0 \geq 1$. As previously demonstrated, this model can be viewed as a non-Hermitian SSH model that is protected by PT-symmetry, and it features purely real eigenvalues and eigenvectors, $|\psi_n^R(k)\rangle$ and $\langle\psi_n^L(k)|$. Therefore, the elements of the projector matrix $P_{\alpha,\beta}(k) = \sum_{n \in \text{occ}} \langle \alpha | \psi_n^R(k) \rangle \langle \psi_n^L(k) | \beta \rangle$ are all real, with α,β labeling the band indices. Upon expanding these elements into real space, and given that $P_{\alpha,\beta}(k)$ are real, we will obtain

$$\langle x_1 | P_{\alpha,\beta} | x_2 \rangle = \sum_k P_{\alpha,\beta}(k) e^{ik(x_1 - x_2)} = \left(\langle x_2 | P_{\alpha,\beta} | x_1 \rangle \right)^*. \tag{S58}$$

Hence, the real-space truncated projector \bar{P} satisfy

$$V\bar{P}V^{-1} = \text{conj}(\bar{P}), \text{ with } V = \begin{pmatrix} 0 & 0 & 0 & \cdots & \mathbb{I} \\ 0 & 0 & \cdots & \mathbb{I} & 0 \\ 0 & \cdots & \mathbb{I} & 0 & 0 \\ \vdots & \vdots & \vdots & \vdots & \vdots \\ \mathbb{I} & 0 & 0 & \cdots & 0 \end{pmatrix},$$
 (S59)

indicating that \bar{P} possesses time-reversal symmetry and its spectrum must consists of complex conjugate pairs (p, p^*) .

In general, for such conjugate pairs of \bar{P} eigenvalues (p, p^*) as $(p_a e^{i\theta_a}, p_a e^{-i\theta_a})$, where p_a, θ_a are real numbers, their contribution to the entanglement entropy can be expressed as

$$S_{\text{pair}} = -p_{a}e^{i\theta_{a}}\log(p_{a}e^{i\theta_{a}}) - (1 - p_{a}e^{i\theta_{a}})\log(1 - p_{a}e^{i\theta_{a}}) -p_{a}e^{-i\theta_{a}}\log(p_{a}e^{-i\theta_{a}}) - (1 - p_{a}e^{-i\theta_{a}})\log(1 - p_{a}e^{-i\theta_{a}}) = 2p_{a}(\theta_{a}\sin\theta_{a} - \log p_{a}\cos\theta_{a}) + 2p_{b}(\theta_{b}\sin\theta_{b} - \log p_{b}\cos\theta_{b}),$$
 (S60)

where p_b, θ_b are defined such that $1 - p_a e^{i\theta_a} = p_b e^{i\theta_b}$. As shown above, $Im(S_{pair}) = 0$, indicating that the entanglement entropy should be a real value. Any imaginary part of the entanglement entropy from computations must be due to numerical errors.

IV. PROSPECTS FOR MEASURING NEGATIVE ENTANGLEMENT THROUGH THE SECOND RÉNYI ENTROPY

From the previous section, it was established that the negative entanglement is also manifested generically as negative Rényi entropy. Below, we outline a scheme for measuring the second Rényi entropy, defined in the biorthogonal basis as:

$$S_A^{(2)} = -\log \text{Tr}[(\rho_A)^2],$$
 (S61)

where the reduced density matrix is given by $\rho_A = \text{Tr}_{\bar{A}} [|\Psi^R\rangle \langle \Psi^L|]$.

A known approach [122–126] for measuring the second Rényi entropy or quantum purity involves the SWAP operator, which exchanges two copies of a quantum state:

$$SWAP |\psi_1\rangle \otimes |\psi_2\rangle = |\psi_2\rangle \otimes |\psi_1\rangle. \tag{S62}$$

A commonly used corollary [127] is $\text{Tr}(\text{SWAP}\rho_1 \otimes \rho_2) = \text{Tr}(\rho_1\rho_2)$, from which the second Rényi entropy can be calculated from the expectation value of the SWAP operator on two-copies of the many body state [122–126, 128] as:

$$\langle \psi | \otimes \langle \psi | \operatorname{SWAP}_A | \psi \rangle \otimes | \psi \rangle = \operatorname{Tr}(\operatorname{SWAP}_A \rho \otimes \rho) = \operatorname{Tr}(\rho_A^2) = e^{-S_A^{(2)}},$$
 (S63)

where SWAP_A denotes the application of the SWAP operator in subregion A. Substituting $\rho = |\Psi^R\rangle \langle \Psi^L|$, we obtain

$$\langle \Psi^{L} | \otimes \langle \Psi^{L} | \operatorname{SWAP}_{A} | \Psi^{R} \rangle \otimes | \Psi^{R} \rangle = e^{-S_{A}^{(2)}}$$

$$\left| \langle \Psi^{L} | \otimes \langle \Psi^{L} | \operatorname{SWAP}_{A} | \Psi^{R} \rangle \otimes | \Psi^{R} \rangle \right| = e^{-\operatorname{Re}[S_{A}^{(2)}]}.$$
(S64)

Therefore, to measure the (real part of the) biorthogonal second Rényi entropy, $\text{Re}[S_A^{(2)}]$, the most mathematically direct way would be to prepare two copies of the ground state of the Hamiltonian H as $|\Psi^R\rangle\otimes|\Psi^R\rangle$, applying the SWAP operator in subregion A, and then measuring its overlap with the ground state $|\Psi^L\rangle\otimes|\Psi^L\rangle$ of another Hamiltonian H^{\dagger} . This approach could potentially be implemented using programmable quantum computers [129–132]. Post-selection, which has been used in measuring negative conditional entropy [63, 64, 133], will also be useful in simulating the non-Hermiticity [38, 134–136].

Alternatively, it would usually be more practical to measure the physical (not biorthogonal) expectation values of the SWAP operator, either as:

$$\langle SWAP_{A} \rangle_{RR} = \langle \Psi^{R} | \otimes \langle \Psi^{R} | SWAP_{A} | \Psi^{R} \rangle \otimes | \Psi^{R} \rangle, \text{ or }$$

$$\langle SWAP_{A} \rangle_{LL} = \langle \Psi^{L} | \otimes \langle \Psi^{L} | SWAP_{A} | \Psi^{L} \rangle \otimes | \Psi^{L} \rangle.$$
(S65)

Thus, to measure $|\langle \Psi^L | \otimes \langle \Psi^L | SWAP_A | \Psi^R \rangle \otimes | \Psi^R \rangle|$ as given in Eq(S64), one feasible strategy is to prepare a superposition state with known amplitudes c_1, c_2 in a physical system:

$$|\Psi\rangle = c_1 |\Psi^R\rangle \otimes |\Psi^R\rangle + c_2 |\Psi^L\rangle \otimes |\Psi^L\rangle, \tag{S66}$$

and then measure the expectation value $\langle \Psi | SWAP_A | \Psi \rangle$. The left-right overlap terms (i.e. Eq(S64)) can subsequently be calculated by subtracting the contributions from $\langle SWAP_A \rangle_{RR}$ and $\langle SWAP_A \rangle_{LL}$, which can also be independently measured. Moreover, the OBC spectrum of our model, as specified in Eq. (9), is purely real, leading to identical energies for $|\Psi^R\rangle$ and $|\Psi^L\rangle$ and thus facilitating the preparation of their superposition.

Beyond the approach described above, other potentially feasible ways for observing negative entanglement can involve directly measuring the reduced density matrix to calculate the entanglement entropy through quantum state tomography [137–139]. Related quantum simulations through quantum Monte Carlo approaches [125, 140, 141] and ultracold atomic optical lattices [122, 123, 142–148] can also reveal the associated quantum correlations.